J. Opt. Fiber. Commun. Rep. 4, 110–172 (2007)

DOI: 10.1007/s10297-007-0081-0
Editors: Siddharth Ramachandran

JOURNAL OF
Optical and Fiber
Communications Reports

High-order mode based dispersion compensating modules using spatial mode conversion

M. Tur[1], D. Menashe[2], Y. Japha[3], and Y. Danziger[4]

[1] School of Electrical Engineering, Tel-Aviv University, Tel-Aviv, Israel 69978
Email: `tur@eng.tau.ac.il`
[2] RED-C Optical Networks, Atidim Tech. Park, Bldg 3, Tel-Aviv, Israel
[3] Department of Physics, Ben-Gurion University of the Negev, Beer-Sheva, Israel 84150
[4] Email: `yochay_danziger@yahoo.com`

Abstract. High-Order Mode Dispersion Compensating Modules (HOM-DCM) using spatial optical transformations for mode conversion are reviewed. It is shown that mode transformers using this technology can be designed to transform the LP_{01} mode of SMF fibers to the LP_{02} mode of specially designed dispersion compensating High-Order Mode Fiber (HOMF), with typical insertion loss of $\sim$1 dB, and typical extinction ratio to other modes less than -20 dB. The HOMF itself can provide high negative dispersion [typically in the range of 400–600 ps/(nm km)], and high negative dispersion slope, allowing efficient compensation of all types of transmission fiber. Combining two mode transformers with HOMF and possibly trim fiber for fine-tuning, results, for example, in a HOM-DCM that compensates 100 km LEAF® fiber, with Insertion loss < 3.5 dB, and Multi-Path Interference (MPI) < -36 dB. MPI phenomena in HOM-DCMs is characterized, and shown to comprise both coherent and incoherent parts, and to result from both the mode transformers and fiber coupling within the HOMF. MPI values of < -36 dB have been shown to allow error free transmission of 10 Gb/s signals over up to 6000 km. Finally, a number of applications well suited to the properties of HOM-DCMs are reviewed.

1. Introduction

In 1994, Craig Poole and coworkers [1–2], as well as others [3], pointed out that High-Order Modes (HOM) in optical fibers, such as LP_{11}, LP_{02}, etc. [4], could be advantageously used for chromatic dispersion compensation. Motivated by the high *negative* dispersion of such modes near their respective cutoffs, as well as by the

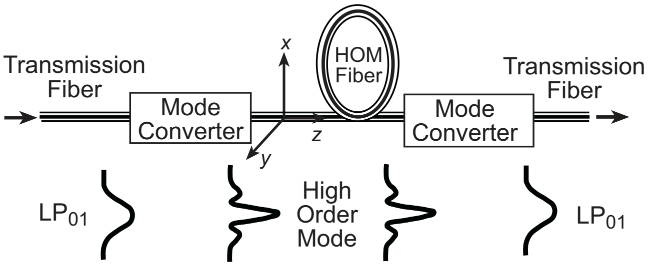

Fig. 1. A High-Order Mode based dispersion compensator. Light propagating in the LP_{01} mode of the transmission fiber is converted to a highly (negative) dispersive high-order mode of a few mode fiber. Finally, the output mode converter sends the light back to the transmission fiber in the form of an LP_{01} mode.

negative slope of the obtained dispersion (with respect to wavelength), Poole et al. have proposed and demonstrated a HOM-based dispersion compensator for SMF28 fiber.

The device, Fig. 1, comprised of a slightly elliptical fiber, carrying the LP_{11} mode, and two broadband mode converters to efficiently transfer the LP_{01} light from the input SMF28 single-mode fiber into the LP_{11}negative dispersion mode, and back into the LP_{01} mode of the output SMF28 fiber. With negative dispersion values as high as -770 ps/(nm km) @ 1555 nm (as compared with ~ -90 ps/(nm km) for regular single-mode Dispersion Compensating Fibers (DCF) [5]), a close to ten-fold saving in fiber length could be achieved with only a relatively small excess loss due to the mode transformers. Poole's reported experimental work has revealed the potential of the technology, although the demonstrated implementation fell short of meeting some key industry requirements (e.g., the use of a slightly elliptical fiber, carrying the LP_{11} mode, could not guarantee polarization insensitivity).

Theoretically, high-order modes introduce a new degree of freedom for dispersion management. They can be designed to have dispersion curves that can match many transmission fibers, including the many Non-Zero-Dispersion-Shifted-Fibers (NZDSF), which were introduced in the last 10 years. The high negative dispersion of HOM fibers (HOMFs) requires much less fiber to achieve a given total dispersion (in ps/nm), resulting in significantly lower loss for the final product. High-order modes are also characterized by large effective areas (50–80 μm^2), much larger than those of dispersion compensating fibers (DCF), which use the LP_{01} mode ($\sim$20 μm^2). While recent advances in basic mode DCF have led to higher values of dispersion and dispersion slope, even comparable to HOMF, these have been achieved at the expense of an even further reduction in effective area, typically to about 15 μm^2[20]. Thus, HOM based dispersion compensators have the potential to be much more immune to optical nonlinear effects, which are to be minimized to ensure successful high channel count WDM, and high capacity 40 Gbs transmission.

In practice, however, a series of obstacles must be overcome before all these advantages can be utilized. The most challenging one is the transformation process between the dispersion compensating HOM and the LP_{01} mode of the transmission fiber. First, this modal transformation has to be very efficient in order to minimize the device insertion loss. But the HOM dispersion compensating fiber is not single-mode, and even if the transformation efficiency is very high, some input optical power may be coupled by the input mode converter to other modes of the HOM fiber (HOMF), including to the always-existing lowest order LP_{01} mode. Mode coupling in the HOMF and/or a non-ideal output mode converter will generate in the *output* transmission fiber multiple electromagnetic fields, which traversed the device via different modes (i.e., different optical paths), resulting in Multiple Path Interference (MPI) (see section 4). Eventually, HOM dispersion compensators are to serve as important building blocks in high performance fiber-optic communication systems, and the above mentioned MPI is the most dominant contribution to system penalty associated with the HOM technology.

A spatial mode of an optical fiber is a solution of Maxwell equations, subject to boundary conditions, having the form [4]

$$\mathbf{E}(x,y,z,t) = \mathbf{E}_0(x,y)\exp(i\beta z)\exp(-i\omega t);$$

$$\mathbf{H} = \mathbf{H}_0(x,y)\exp(i\beta z)\exp(-i\omega t). \tag{1}$$

Here, **E** and **H** are the vector electromagnetic fields, t is the time and ω is the optical (angular) frequency, z is a coordinate along the fiber length, while x and y are the transverse spatial coordinates, see Fig. 1, $\mathbf{E}_0(x,y)$ and $\mathbf{H}_0(x,y)$describe the z-independent mode transverse shape, and finally, β is the propagation constant. Modes differ from each other in their transverse field distributions $\mathbf{E}_0(x,y),\ \mathbf{H}_0(x,y)$and propagation constant β.

In the so-called weakly guiding approximation, modes in cylindrically symmetric fibers are classified using the LP_{mn} designation [6] , where LP stands for "linearly polarized", m represents the azimuthal symmetry of the mode, and n the radial distribution. Figure 2 shows typical spatial distributions of the electromagnetic *field* (not intensity) of the modes, most relevant to the design of HOMF for dispersion compensation. The basic mode LP_{01}, exclusively used for high bit-rate transmission, is cylindrically symmetric, and its radial distribution is approximately Gaussian. The LP_{02}, and LP_{03} modes are also cylindrically symmetric, however their radial distribution has one and two zero-amplitude rings, respectively, i.e. points where the electric field changes sign. The LP_{11} and LP_{21} modes are not cylindrically symmetric, having two and four lobes respectively. Besides their different spatial distributions, modes are further characterized by the their effective index n_{eff}, or alternatively by the propagation constant $\beta = kn_{\mathrm{eff}}$, where $k\ (=\omega/c)$ is the vacuum wave-number (c is light velocity in vacuum). Since $n_{\mathrm{core}} > n_{\mathrm{eff}} > n_{\mathrm{clad}}$, where n_{core} and n_{clad} are respectively, the refractive indices of the fiber core and cladding, the larger n_{eff} the more guided and stable the mode. Figure 3 shows the n_{eff} values for a typical HOM fiber to be discussed in section 3.

LP_{01}has the highest n_{eff}, with n_{eff} decreasing according to the following typical order LP_{11}, LP_{21}, LP_{02}, LP_{12}, LP_{03}, LP_{22}. The number of guided modes in the fiber is equal to the number of modes for which $n_{\mathrm{eff}} > n_{\mathrm{clad}}$, where n_{clad} is the index of the fiber cladding material (typically undoped Silica, with n_{clad} = 1.444 @ 1550 nm).

The vast majority of fibers in commercial use today may be divided into two distinct categories: single and multi-mode fibers [4]. In single mode fibers, only the

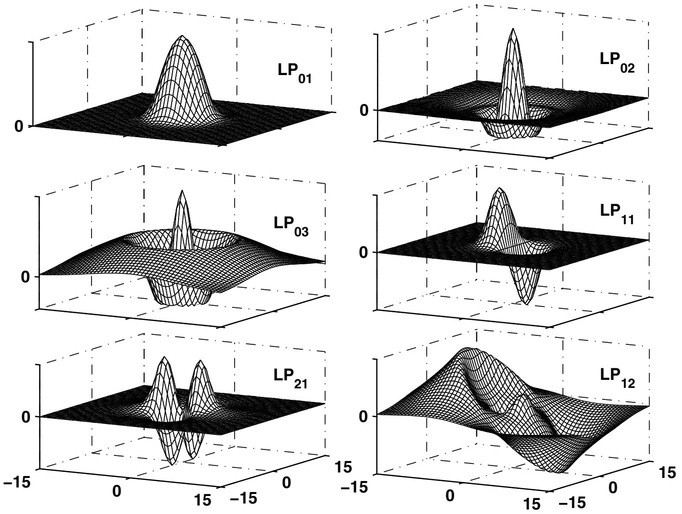

Fig. 2. Typical spatial *field* distribution of selected modes of a HOM fiber.

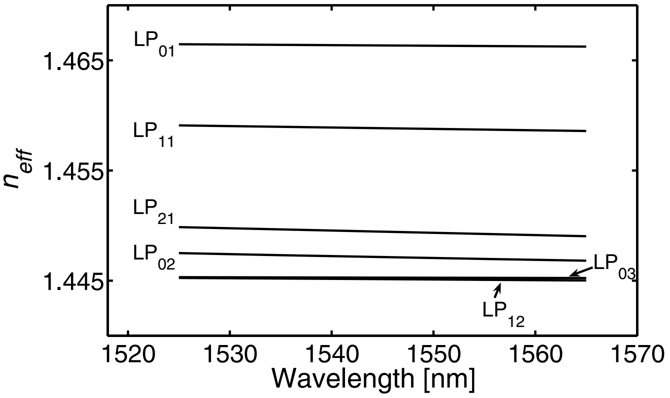

Fig. 3. Typical $n_{\rm eff}$ values for the modes of Fig. 2 (Δ_1=0.027, see section 3).

LP_{01} is guided for wavelengths exceeding a cutoff value. On the other hand, a multimode fiber (MMF) supports a multitude of guided modes, with the signal propagating simultaneously in all (or in some cases a subset) of the modes. The term HOMF used here refers to a subclass of the multimode family, also being referred to as few-mode fibers [7]. These fibers are designed to support a limited number of guided modes (typically less than ten), with the signal designated to propagate in a pre-selected *single* high-order mode.

To selectively couple the input LP_{01} to the HOMF LP_{11} mode and back, Poole et al. have used grating coupling to introduce longitudinal periodic perturbations in the core region of the fiber with a spatial period matched to the intermodal beat length $L_B = 2\pi/(|\beta_{01} - \beta_{11})$ (β_{01} and β_{11} are the propagation constants of the LP_{01} and LP_{11} modes, respectively). This grating method has been further perfected in recent years by Ramachandran et al. [8–9]. Recently, another method for mode conversion using hollow fibers has also been proposed [10].

In 1998 one of the authors of this paper (Y. D.) proposed to replace the *one-dimensional* selectivity of β matching by a *two-dimensional* mechanism, where the spatial shape, $\mathbf{E}_0(x, y),\ \mathbf{H}_0(x, y)$ of the transmission fiber LP_{01} mode is transformed by a two-dimensional spatial filter into the precise $\mathbf{E}_0(x, y),\ \mathbf{H}_0(x, y)$ field distribution of the desired high-order mode and *vice versa*. Reshaping laser beams by diffractive optical elements has been a known practice for years, but only lately it was utilized for modal transformation [11]. In this paper we demonstrate how mode transformers (MOXes) based on spatial wavefront transformation, combined with appropriately designed HOMF, can achieve:

- Broadband, continuous and full (including slope) compensation over the transmission band of wavelengths (e.g., the C (1525–1565 nm) or L (1570–1610 nm) bands
- Low insertion loss
- Low polarization mode dispersion (PMD) and polarization dependent loss (PDL) [6]
- High tolerance to optical power
- Low return loss
- Low MPI
- Compact size and full compatibility with Telcordia requirements from a passive device

Higher-Order-Mode Dispersion Compensation Modules (HOM-DCMs) based on this technology have been developed and built by LaserComm, Inc. to meet all the stringent requirements of modern and future high performance fiber optic telecommunication systems.

Paper structure: section 2 describes the design and construction of a *spatial* mode transformer. The trade-off considerations in the design of the HOM fiber itself are discussed in section 3, while MPI is the subject of section 4. The overall performance of the integrated HOM-DCM is presented in section 5 along with numerous potential applications, and its success in various field experiments.

2. Spatial Mode Transformer (MOX)

2.1. General

Mode transformation is needed in order to transfer the signal in the incoming single-mode transmission fiber into a higher order transverse mode of the dispersion compensating fiber. An inverse mode transformation is then invoked to transfer the signal

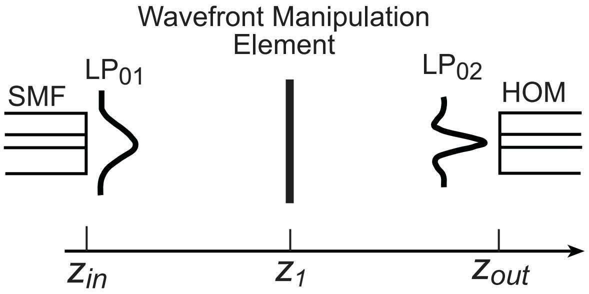

Fig. 4. Transformation from the Gaussian LP_{01} mode of an SMF to the LP_{02} mode of a HOM fiber.

back into the single-mode output transmission fiber. The transmission fiber is usually a single-mode fiber (SMF), with a Gaussian shape transverse mode, LP_{01}, while the HOMF is a few mode fiber, supporting a high-order spatial transverse mode, designed to have a prescribed high negative dispersion curve. For a variety of reasons to be discussed in section 3, we chose to work with the cylindrically symmetric *non-degenerate* LP_{02} high-order mode, whose schematic field distribution, $E_{02}(x,y)$, is shown in Fig. 2 (in the weakly guiding approximation [4], the polarization is uniform across the (x,y) plane and its value will be that of the incident LP_{01} wave). Note that unlike LP_{01}, $E_{02}(x,y)$ for LP_{02} has a cylindrically symmetric π radians phase shift around its central lobe. As discussed above, the challenge in designing a good spatial mode transformer is twofold: (a) to transfer a maximum fraction of the energy of the input mode into the desired output mode, i.e., to have a minimum insertion loss; (b) to minimize excitation of other guided modes in the HOM fiber in order to prevent undesired interference effects at the HOM-DCM output fiber (MPI, see section 4). This challenge should be successfully met over a broad spectrum of wavelengths and environmental conditions.

2.1.1. Principles of Spatial Mode Transformation

Spatial mode transformation is based on wavefront manipulation using specially designed optical elements and free-space propagation. Since the input fiber modes are weakly guided and the optical beams will be seen to have only small to moderate divergence/convergence angles, we may assume that for incoming linearly polarized light, all optical beams in free space will share the same polarization, with the electric field component along the polarization axis described by a *scalar* complex function of the form

$$E(x,y,z,t) = f(x,y,z)\exp(-i\omega t). \tag{2}$$

Using scalar diffraction theory [12,13], free space propagation of the electric field from plane z_1 to plane z_2 is governed by

$$f(x,y,z_2) = \iint dx'dy'G(x-x',y-y',z_2-z_1)f(x',y',z_1), \tag{3}$$

where the Green's function $G(\cdot)$ in the Fresnel approximation is given by [12]

$$G(x-x', y-y', z-z') = \frac{i}{\lambda\,|z-z'|}\exp\left(-i\frac{\pi}{\lambda\,|z-z'|}[(x-x')^2+(y-y')^2]\right), \tag{4}$$

The field at any given distance z, $f(x,y,z) = \sqrt{I(x,y,z)}\exp(i\varphi(x,y,z))$ has intensity profile $I(x,y,z)$ and phase $\varphi(x,y,z)$. Through theory and/or measurements we know the fields of the input and output modes at $z = z_{\text{in}}$ and $z = z_{\text{out}}$, respectively, Fig. 4. Using Eq. (3) we can forward propagate $f(x,y,z_{\text{in}})$ of the input mode to get its value$f(x,y,z_1^-)$, just before the assumingly relatively thin transforming element, and reverse propagate $f(x,y,z_{\text{out}})$ of the output mode to just after the transforming element to produce the wavefront$f(x,y,z_1^+)$, that will converge to $f(x,y,z_{\text{out}})$ through free space propagation. Successful mode conversion can be achieved by placing an optical element at $z = z_1$, having a complex transfer function

$$H(x,y) = T(x,y)\exp(i\Phi(x,y)) = |H(x,y)|\exp(i\Phi(x,y)), \tag{5}$$

such that

$$f(x,y,z_1^+) \propto H(x,y)f(x,y,z_1^-). \tag{6}$$

Thus, up to a constant of proportionality, i.e., allowing for some spatially uniform insertion loss, the mode of the left-hand fiber is spatially matched to that of the right-hand one, as required. In practice, however, this approach is problematic: while the $\exp(i\Phi(x,y))$ part of $H(x,y)$ of Eq. (6) could be implemented using a *phase-only* optical element, which can be made today to high precision [14] , absorptive masks, performing the wavefront transformation prescribed by $|H(x,y)|$, are more difficult to manufacture. Moreover, the use of an absorptive element may entail considerable insertion loss.

An alternative approach is to use an optical system, comprising two phase-only thin elements at z_1 and z_2, Fig.5, combined with free space propagation between the z_1 and z_2 planes to convert the phase variations imposed at z_1 to intensity variations at z_2. In fact, it may be shown [15] that for a suitable choice of distances, $z_1 - z_{\text{in}}$, $z_2 - z_1$ and $z_{\text{out}} - z_2$, any wavefront transformation between the planes z_{in} and z_{out} can be implemented by phase-only wavefront manipulation at z_1 and z_2. The required phase elements can be designed using a phase retrieval algorithm, described in section 2.2.3.

2.1.2. The Need for Collimation

The proposed mode transformer must also possess significant optical (focusing) power, since it must collect the diverging beam, emanating from the left-hand fiber and transform it into an appropriately modified converging beam into the right-hand fiber. For easy implementation, and to keep the phase elements as *thin* and *shallow* as possible, it is preferable to assign the required optical power to collimating and focusing lenses, L1 and L2 in Fig. 6. Although quite a few other mode transformer architectures can be also envisaged, in the following we concentrate on the architecture of Fig. 6, and in particular on the $\text{LP}_{01} \rightarrow \text{LP}_{02}$ transformation.

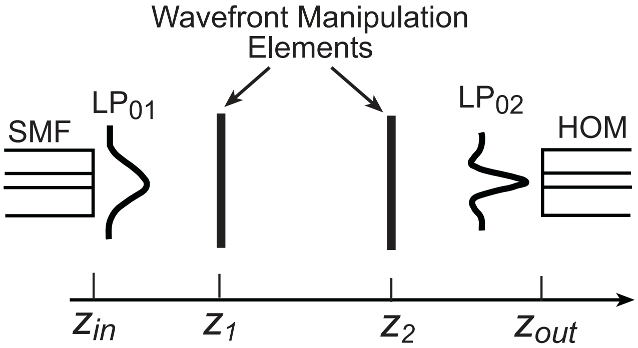

Fig. 5. Same as Fig. 4 but with two thin phase elements to execute the required mode transformation.

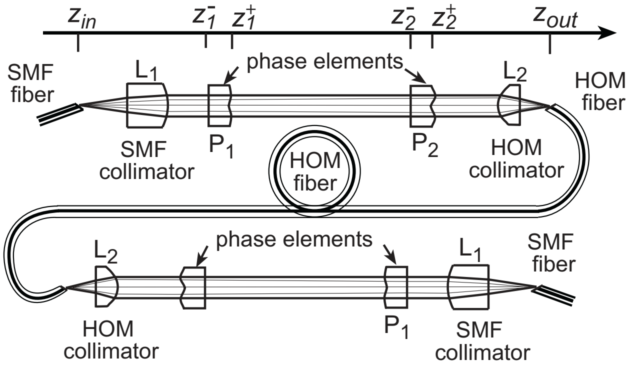

Fig. 6. Typical architecture of a HOM-DCM with both input and output MOXes to be discussed below. Ray tracing shows how intensity is spread into a central lobe and outer ring near the P2 phase elements. The SMF-28 fiber ends are cut at an angle of 8°, and consequently, the fiber mechanical axis forms an angle of ∼3.6° with the MOX optical axis, see section 2.2.1.

2.1.3. Efficiency of the Spatial Transformation

Starting with the normalized field $f_{01}(x, y, z_{\rm in})$ of the LP$_{01}$ mode at $z = z_{\rm in}$, the output of the optical system of the input MOX of Fig. 6 is a transformed field $f_{\rm trans}(x, y, z_{\rm out})$ at the input facet of the HOM fiber (inside the fiber so that reflection losses are taken into account). The fraction of power coupled into a specific fiber mode LP$_{mn}$, having a normalized mode field $f_{mn}(x, y)$ is given by $|A_{mn}|^2$, where the amplitude A_{mn} can be evaluated from the overlap integral

$$A_{mn} = \int dxdy f^*_{mn}(x, y) f_{\text{trans}}(x, y, z_{\text{out}}). \tag{7}$$

The MOX is designed to perform ideal transformation at the design wavelength λ_0, which is typically at the center of the transmission band. For this wavelength, $|A_{mn}|^2$ should be unity for the desired mode (excluding losses in the optical system), and zero for all other modes. However, the transformation is not ideal at wavelengths away from the central wavelength λ_0, and in addition, imperfections in the MOX manufacturing cause the transfer of power into some undesired modes.

2.1.4. Definitions

The insertion loss of an $\text{LP}_{01} \rightarrow \text{LP}_{02}$ MOX is defined as

$$\text{Insertion Loss(IL)} = -10 \log_{10} |A_{02}|^2 \ , \tag{8}$$

The extinction ratio (ER) of the undesired mode LP_{mn} $((m, n) \neq (0, 2))$ is defined as

$$\text{ER}_{mn} = 10 \log_{10} \left[\left| \frac{A_{mn}}{A_{02}} \right|^2 \right]. \tag{9}$$

Obviously, a high *efficiency* MOX is characterized by an insertion loss of close to zero dB and extinction ratio approaching $-\infty$ dB, over the full wavelength band of operation.

The *broadband* efficiency of the transformation is limited by two main factors:

- The chromatic aberrations of the optical system, caused by either material dispersion of the elements or wavelength-dependent diffractive effects.
- The wavelength dependence of the wavefronts $f_{01}(x, y, z_{\text{in}})$ and $f_{02}(x, y, z_{\text{out}})$ of the LP_{01} mode of the transmission fiber and LP_{02} mode of the HOM fiber, respectively.

One would expect the diffractive effects in the optical elements to present an obstacle to broadband operation. However, this problem can be minimized by using smooth phase elements with mostly refractive nature, in the sense that they do not have the 2π phase jumps typical of regular diffractive elements [13]. Material dispersion in the optical elements is important but in principle can be compensated for using conventional achromatization techniques [13].

The main limitation is then modal shape dispersion of the HOM fiber. While the wavelength dependence of the incoming LP_{01} modal shape $f_{01}(x, y, z_{\text{in}})$ can be shown to be insignificantly small, the whole idea of choosing a high-order mode was because of its high group velocity dispersion, see section 3. It is to be expected, therefore, that $f_{02}(x, y, z_{\text{out}})$ might also have considerable wavelength dependence, posing significant limitations to the transformation efficiency. However, it turns out that for dispersion values in the range of practical interest, about 200–600 ps/nm/km, the rate of change of the HOMF mode shape is still small enough to allow efficient and broadband spatial mode transformation. To illustrate this point consider an achromatic optical system designed for ideal transformation at $\lambda = 1550$ nm, with wavelength-independent $f_{01}(x, y, z_{\text{in}})$. The insertion loss of the desired mode and the extinction ratio for the undesired modes are then obtained from an overlap integral of the desired

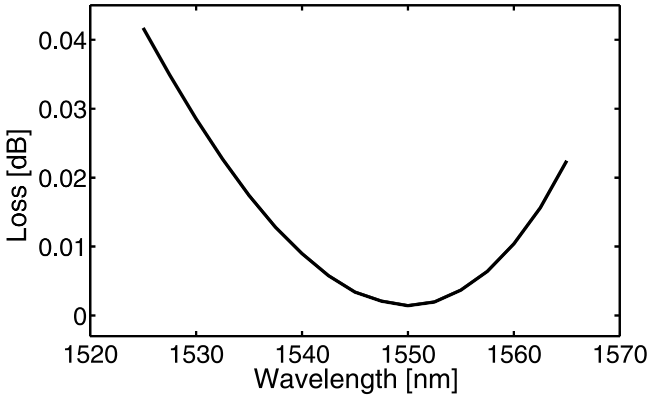

Fig. 7. LP_{02} loss over the C-band for a typical HOM fiber due to the spectral dependence of the transverse shape of the LP_{02} mode.

mode function $f_{02}(x, y, z_{\mathrm{out}})|_{\lambda_0}$ at $\lambda_w = 1550$ nm (since this is the incident wavefront at the entrance of the HOM fiber) with the corresponding modes of the HOM fiber at the other wavelengths. These quantities are shown in Figs. 7 and 8 for the transformation to the mode LP_{02}, as well as to the undesired modes LP_{01} and LP_{03} for a typical dispersion compensating HOMF of section 3 (Dispersion for this fiber at 1555 nm is -230 ps/(nm km) and dispersion slope is –3.5ps/(nm^2 km)). It is clearly seen that IL does not deteriorate by more than 0.07 dB over the whole C band, while the ER of LP_{01} is at most -40 dB per MOX. The ER for LP_{03} is worse but not so important for properly designed HOMF, since this mode can be removed by fiber bending (see section 3.4.2.2). Finally, in principle it is possible though difficult, to intentionally design some chromatic aberration into the optical elements to somewhat compensate for the wavelength dependence of the HOMF modal shapes.

2.2. *Details of the MOX Architecture*

Here we give a more detailed description of the MOX architecture of Fig. 6.

2.2.1. The Fiber Ends

The fiber ends are mounted into a ferrule, and to reduce back-reflections, cleaved and polished at an angle of 8° (for the SMF-28). Due to Snell's law of refraction, the beam coming out of the fiber creates an angle of $11.6^0$with the polished face, so that the mechanical axes of both ferrules have to be adjusted to deviate from the MOX optical axis by 3.6°. The tilt angles for the HOMF, as well as the resulting back-reflections will be discussed in section 2.3.4.

2.2.2. The Collimators

The SMF collimator lens L1, Fig. 6, is designed to transform the diverging LP_{01} output of the transmission fiber into a collimated beam, while on the HOM fiber side,

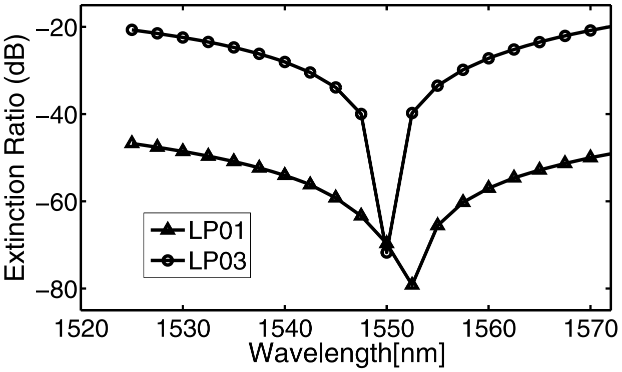

Fig. 8. Extinction ratio for the LP_{01} and LP_{03} modes over the C-band for a typical HOM fiber due to spectral dependence of the transverse shape of the LP_{02} mode.

the purpose of lens L2 is to refocus the beam into the HOMF. Conversely, for the $\mathrm{LP}_{02} \rightarrow \mathrm{LP}_{01}$ MOX, L2 collimates the beam emanating from the HOMF, while L1 refocuses it into the transmission fiber. When a propagating mode exits the fiber into free space, the beam starts to diverge. The distribution of angles from a given mode (the angular power spectrum) is given by the following Fourier transform over the transverse mode function $f(x, y)$:

$$g(\theta,\varphi) \propto \left| \iint dxdy \exp\left(i\frac{2\pi}{\lambda}\sin\theta(x\cos\varphi + y\sin\varphi)\right) f(x,y) \right|^2, \qquad (10)$$

where θ and φ are spherical angles in free space in the xyz coordinate system of Fig. 1. The numerical aperture of a beam is defined [13] as the width of the angular spectrum distribution, or more precisely: the sine of an angle θ_{NA} such that a specified fraction (e.g. 1/e^2 or 99%) of beam power is contained in a cone, having an opening angle of $2\theta_{\mathrm{NA}}$. Owing to their dissimilar modal fields, the NA's of LP_{01} and LP_{02} are quite different, with that of the LP_{02} significantly larger (ranging between 0.36 and 0.42) than that of LP_{01} (NA = 0.155).

The focal length of a lens dedicated for the collimation of a beam with a given NA into a collimated beam with diameter D is given by

$$f = \frac{D}{2\mathrm{NA}}. \qquad (11)$$

To ease environmental stability, all MOX dimensions should be chosen as small as possible but large enough so that the manufacturing resolution of the phase elements enables the capturing of all the spatial details needed for a precise spatial transformation. This includes the diameter D of the collimated beam. Typically, D can be of the order of a few millimeters. Since fairly little beam divergence occurs between L1 and L2 (Typically, the length of an assembled MOX is a few centimeters), L2 can also be of diameter D, but due to the different NA's, its focal length is shorter than that of

L1 by the NA's ratio. Clearly, L1 and especially L2 are high NA lenses and should be manufactured to high standards of accuracy.

2.2.3. The Phase Elements

The phase elements play the most important role in the spatial mode transformation. As described above, a pair of phase elements is needed to perform the transformation. The first phase element P1 adds a phase to the input beam such that the free-space propagation through the air gap to the face of the second phase element P2 creates an intensity profile, matching the intensity profile of the desired output beam at the side of the HOM fiber. The second phase element P2 adds another phase such that the intensity and phase of the resulting field matches the intensity and phase of the desired HOM fiber mode, when focused onto the end-face of the HOM fiber.

Phase elements can be manufactured using transparent dielectric disks with position- dependent thickness, or 'height'. A dielectric element with refractive index n and a curved surface of height $h(x,y)$ adds an optical phase

$$\Phi(x,y) = \frac{2\pi}{\lambda}(n-1)h(x,y) \tag{12}$$

to an incident beam of light (n is the refractive index of the material from which the phase elements are made).

An iterative algorithm for the design of the phase elements is based on the phase retrieval algorithm, known also by the "pendulum" or "ping-pong" algorithm [15]. The design of phase elements P1 and P2 starts after their locations, z_1 and z_2, have been selected (based on various mechanical and optical criteria), and comprises the following steps:

1. Based on the wavefront of the LP$_{01}$ mode at the input SMF end face, $f_{01}(x,y,z_{\text{in}})$, and the detailed design and focal distance of the collimating lens, L1 (see Fig. 5 and the upper part of Fig. 6) calculate the collimated field $f_{01}(x,y,z_1^-) = \left|f_{01}(x,y,z_1^-)\right| \exp[i\phi_{01}(x,y)]$ incident on P1 at $z = z_1^-$ (The subscript 01 is used to emphasize that both the amplitude and phase of this field are determined by the mode shape of the input fiber and they will *not* change during the iterations). Similarly, by reverse-propagating the LP$_{02}$ wavefront, $f_{02}(x,y,z_{\text{out}})$ from the HOM end face, through the focusing lens, L2, and to $z = z_2^+$, we obtain the collimated target field $f_{02}(x,y,z_2^+)$, which should leave P2 at $z = z_2^+$ in order to perfectly excite LP$_{02}$ at the input of the HOM fiber. Again, both the amplitude and phase of this wavefront, $f_{02}(x,y,z_2^+) = \left|f_{02}(x,y,z_2^+)\right| \exp[i\phi_{02}(x,y)]$, will not change during the iterations.
2. Start an iterative process by first setting the optical phase added by P1 to be $\Phi_{P1}(x,y) \equiv 0$.
3. Add the phase $\Phi_{P1}(x,y)$ to the field $f_{01}(x,y,z_1^-)$ to obtain a forward propagating wavefront $f_{\rightarrow}(x,y,z_1^+) = f_{01}(x,y,z_1^-)\exp[i\Phi_{P1}(x,y)]$ at the output of P1.
4. Use the Fresnel formula, Eq. (3), to propagate the field $f_{\rightarrow}(x,y,z_1^+)$ from z_1^+ to z_2^- and obtain the field distribution at the input of P2, $f_{\rightarrow}(x,y,z_2^-)$, whose phase is $\phi(x,y,z_2^-)$, i.e., $f_{\rightarrow}(x,y,z_2^-) = \left|f_{\rightarrow}(x,y,z_2^-)\right| \exp[i\phi(x,y,z_2^-)]$.

5. Define the phase to be added by P2 to be $\Phi_{P2}(x, y) = \phi_{02}(x, y) - \phi(x, y, z_2^-)$s which is the difference between the spatial phases of wavefronts before and after P2. By the very definition of $\Phi_{P2}(x, y)$, the field emerging from P2 matches the correct field $f_{02}(x, y, z_2^+)$ in phase, but its amplitude: $\left|f_{\rightarrow}(x, y, z_2^+)\right| = \left|f_{\rightarrow}(x, y, z_2^-)\right|$ does not necessarily equal that of the target field $f_{02}(x, y, z_2^+)$! To correct for that we proceed with a backward iteration:
6. Impose the amplitude of $f_{02}(x, y, z_2^+)$ on the field at $z = z_2^-$ by subtracting $\Phi_{P2}(x, y)$ from the collimated HOM field $f_{02}(x, y, z_2^+)$ to obtain a new estimate for the field at $z = z_2^-$: $f_{\leftarrow}(x, y, z_2^-) = f_{02}(x, y, z_2^+) \exp[-i\Phi_{P2}(x, y)]$ (note the backward arrow subscript).
7. Reversepropagate this field from $z_2^-$to z_1^+ and obtain the field distribution $f_{\leftarrow}(x, y, z_1^+) = \left|f_{\leftarrow}(x, y, z_1^+)\right| \exp[i\phi(x, y, z_1^+)]$.
8. Assign a new value to $\Phi_{P1}(x, y)$, using $\Phi_{P1}(x, y) = \phi(x, y, z_1^+) - \phi_{01}(x, y)$. Again, we have matched the phase of the calculated field with that of the known input field $f_{01}(x, y, z_1^-)$, but the amplitude of $f_{01}(x, y, z_1^-)$ may not match that of the calculated field $\left|f_{\leftarrow}(x, y, z_1^-)\right| = \left|f_{\leftarrow}(x, y, z_1^+)\right|$. Therefore,
9. Using the updated $\Phi_{P1}(x, y)$, go back to step 3 and iterate until $\Phi_{P1}(x, y)$ and $\Phi_{P2}(x, y)$ converge to stable values.
10. Determine the surface heights of phase elements P1 and P2 from the phases $\Phi_{P1}(x, y)$ and $\Phi_{P2}(x, y)$ using Eq. (12).

The procedure may result in surface heights with sub-micron spatial detail (in the $\{x, y\}$ plane). However, a spatial smoothing procedure is recommended in each step of this algorithm, see section 2.2.4.

The phase $\Phi(x, y)$ is defined up to an integer multiple of 2π, so that one may use either a continuous function or a piecewise continuous function with 2π phase jumps. The first option is much more favorable for broad spectral response, since discontinuous optical elements have significant chromatic aberrations [13]. For a transformation between the cylindrically symmetric modes LP_{01} and LP_{02}, cylindrically symmetric phase elements are used. Such phase elements may be manufactured by relatively cheap diamond turning techniques. The curved surfaces of P1 and P2 face each other, such that the transformation is done in the air gap between them.

Figure 9 shows the surface height of the phase elements P1 and P2 of a typical MOX at a section through their centers. The role of phase element P1 may be understood in terms of geometrical optics. It consists of a central convex part, which resembles a lens. This convex part is responsible for focusing the central part of the incident Gaussian-shaped beam to the central lobe of the soon-to-become LP_{02} mode. The outer ring of P1 transforms the outer part of the incident beam into the outer ring of the LP_{02} mode. Free space propagation between P1 and P2 generates the required intensity pattern at P2, as well as some phase distribution. P2 contributes the final phase correction, and in particular, it introduces a sharp phase step ofπ radians between the inner and outer parts of the element to faithfully reproduce the negative outskirts of the LP_{02} mode of the HOM fiber. For a $\text{LP}_{02} \rightarrow \text{LP}_{01}$ MOX, the π phase shift flips the sign of the negative part of the LP_{02} mode, such that the lobe and ring parts have the same sign, as dictated by the Gaussian shape of the LP_{01} mode. Again, the central part of P2 maps the central LP_{02} lobe into the central part of the Gaussian LP_{01}, and P2 outer part focuses the ring part of LP_{02} into the outer part of the Gaussian. An example of the evolution of the field along the axis of the MOX is given in Fig. 10.

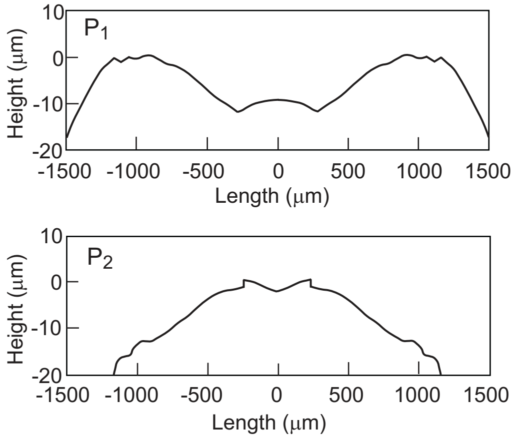

Fig. 9. Sections through the center of the surface heights of the phase elements P1 and P2.

2.2.4. Design Considerations

2.2.4.1. Surface Smoothness

The accuracy of the transformation at the design wavelength is limited by how accurately the designed surface, $h(x, y)$, can be manufactured. Conventional and relatively low cost manufacturing techniques, such as diamond turning, have transverse resolutions of the order of 30-40 μm. Thus, the designed $h(x, y)$ should always be smoothed to comply with the available manufacturable resolution. A smoothed design also offers low sensitivity to alignment and collimation imperfections, wavelength dependence and environmental conditions. On the other hand, a too-smoothed surface may hurt the accuracy of the required wavefront transformation, resulting in lower MOX efficiency in terms of both IL and ER. In practice, a balance can be achieved between sufficient broadband accuracy and stable and robust performance.

2.2.4.2. Transformation Distance

The transformation distance $|z_2 - z_1|$ should be large enough so that the phase variation introduced by P1 will have enough distance to translate into the desired intensity of the target beam. However, it should be kept short enough to minimize chromatic and thermal effects. An optimum distance may be achieved by consecutive applications of the design algorithm with different trial distances.

2.3. MOX Imperfections

The performance of the MOX may be characterized by its insertion loss and its extinction ratio, as well as by its PMD (polarization mode dispersion), PDL (polarization dependent loss), return loss and stability of performance over the required spectral

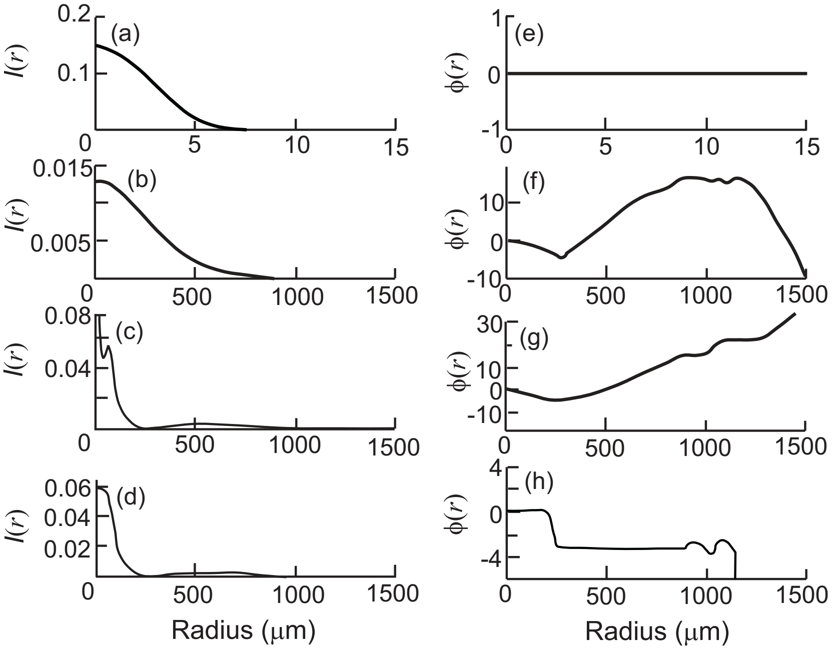

Fig. 10. Radial shape of the field at some planes along the MOX. The intensity (left, arbitrary units) and the phase (right, radians) of the field are shown (from top to bottom) at the SMF fiber end [(a) and (e)], after phase element P1 [(b) and (f)], just before phase element P2 [(c) and (g)] and after P2 [(d) and (h)]. The field diameter after collimation grows by a factor of about 100. After P2 the phase of the field assumes a π phase jump at about $r = 200$ μm. The absolute value of the phase here is not important.

band under industry standard environmental conditions. As discussed in section 2.1.3, wavelength dependence of the mode shape puts a theoretical upper limit on the broadband MOX performance. However, in practice, most of the insertion loss and leakage of power into undesired modes is caused by alignment errors and imperfections in manufacturing, as well as by temperature effects.

2.3.1. Chromatic Aberrations of the Optical System

The use of optical elements without discontinuous jumps minimizes their chromatic dependence. The main contribution of the optical components to the wavelength dependence of MOX performance is then due to chromatic aberrations caused by material dispersion of the optical elements, having relatively high optical power, namely, the lenses. The change in the focal length, f, of a thin lens with refractive index n, may be approximated by

$$\frac{\partial f}{\partial \lambda} \approx \frac{f}{n-1}\frac{\partial n}{\partial \lambda}. \tag{13}$$

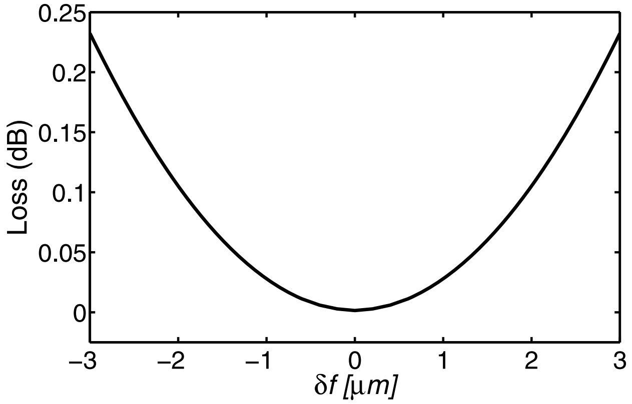

Fig. 11. Insertion loss as a function of defocusing at the HOMF side.

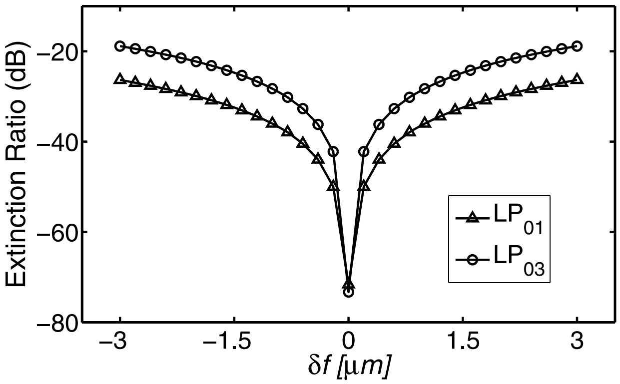

Fig. 12. Extinction ratio as a function of defocusing at the HOMF side.

For typical numbers of $\partial n/\partial\lambda = -0.01\ \mu\text{m}^{-1}$, n=1.5 and f ∼3 mm, we obtain $\delta f \approx \pm 1.5\ \mu$m over the C transmission band. Figures 11 and 12 show the loss and extinction ratio for modes LP_{01} and LP_{03} as a function of the defocusing length δf at the HOM fiber end.

The sensitivity of the transformation to defocus at the SMF end is much smaller. However, a combination of defocus at the SMF and the HOM ends may be used to compensate for aberrations during MOX assembly, as described in section 2.4.2.

The overall wavelength dependence of the loss and extinction ratio of the MOX is shown in Figs. 13 and 14. The plotted curves represent the results of a theoretical simulation that takes into account the combined effects of the fiber modal shape dispersion and the chromatic aberrations of all optical elements. We see that the effect of

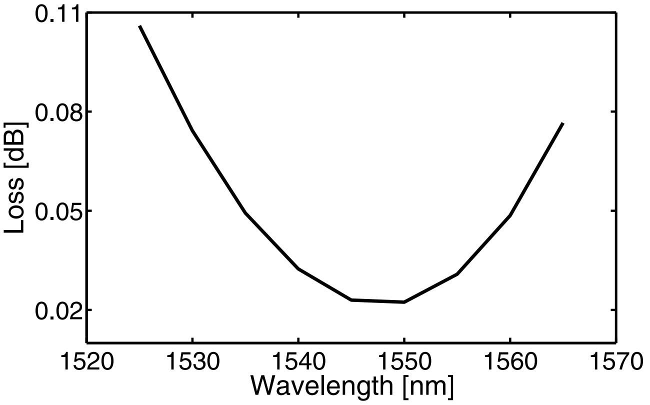

Fig. 13. Theoretical loss of the MOX as a function of wavelength in the C band.

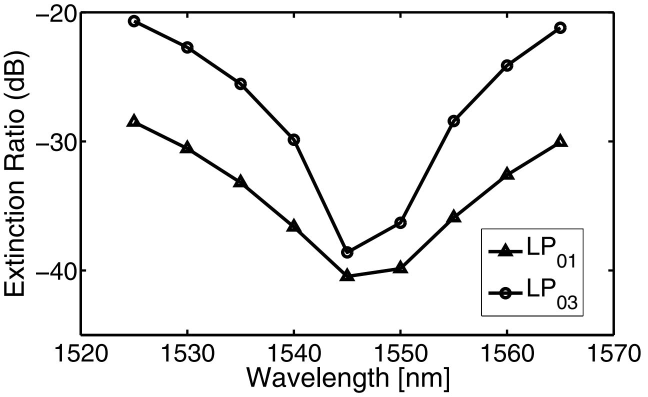

Fig. 14. Theoretical wavelength dependence of the extinction ratio for the modes LP_{01} and LP_{03}.

the chromatic aberrations is of the same order of magnitude as the effect of the modal shape dispersion, cf., Figs. 7 and 8.

2.3.2. Achromatic Aberrations of the Optical System

Achromatic aberrations of the optical system may be caused either by manufacturing-induced imperfections of the optical elements and fiber ends, or by imperfections in the manual or automated assembly of the MOX. The aberrations may be divided into a few groups:

Cylindrically symmetric aberrations, such as defocus or spherical aberrations: This kind of aberrations is responsible for the excitation of cylindrically symmetric fiber modes, such as LP_{01}, LP_{03} etc. These aberrations can be partially compensated for by

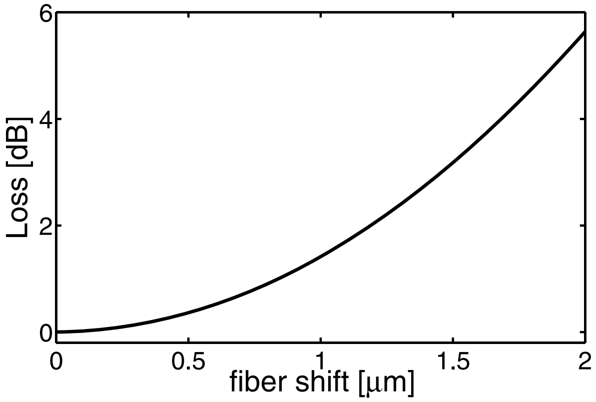

Fig. 15. Theoretically calculated insertion loss of the MOX due to a transverse shift of the HOM fiber end from its center position.

the movement of the fiber end along the lens axis. An example of the effect of defocus on the loss and ER of the MOX is shown in Figs. 11 and 12, respectively.

Antisymmetric aberrations, such as tilt or coma, which are antisymmetric about the x or y axes: These aberrations cause the excitation of antisymmetric modes, such as LP_{11}. They may be partially compensated for by moving the fiber end perpendicular to the optical axis. Examples of the effect of a transverse shift on the insertion loss and on the excitation of higher order modes, other than the LP_{02} mode, are shown in Figs. 15 and 16.

Elliptical aberrations such as astigmatism, where the phase is symmetric about the x and y-axis but not cylindrically symmetric: Such aberrations cause the excitation of modes such as LP_{21}. Usually, this kind of aberration is difficult to compensate during assembly and should be avoided.

The main *practical* cause of aberrations is due to imperfect manufacturing of the phase elements. Very careful collimation and alignment of the optical elements is needed in order to partially compensate for these aberrations. If the process of assembly is not done very carefully, then the main cause of additional aberrations may be tilts and shifts of optical elements. Automated assembly processes can alleviate most of these problems, producing MOXes of the required quality.

2.3.3. Combination of Chromatic and Achromatic Aberrations: The Appearance of Wavelength Dependent Loss

As discussed above, the main chromatic aberration is a wavelength dependent defocus. If a defocus exists in the system at the central wavelength then this defocus adds to the chromatic defocus to create wavelength dependent loss (WDL). An example of the appearance of WDL for a system with defocus is shown in Fig.17.

WDL can be minimized to below 0.1 dB over the C-band. However, by playing with the MOX collimation (changing the defocus) one can choose a specific wavelength

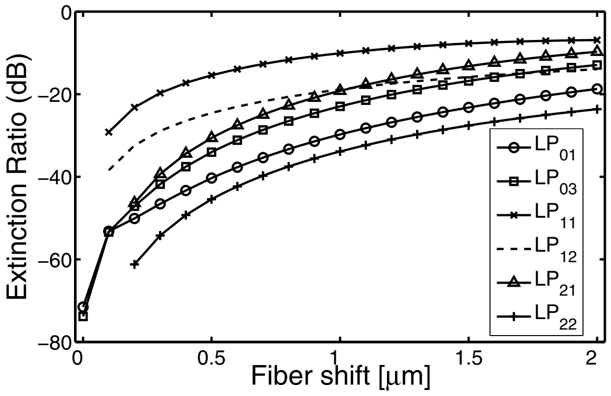

Fig. 16. Theoretically calculated extinction ratios of some guided modes (excluding) LP_{02}, caused by a transverse shift of the HOM fiber end from its center position.

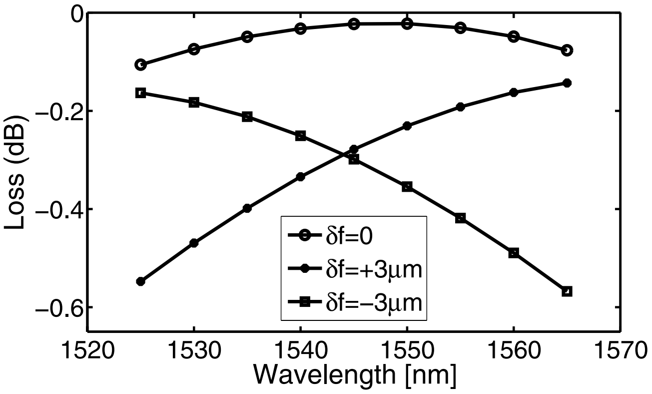

Fig. 17. Wavelength dependent loss (WDL) of the MOX caused by a longitudinal shift $df = \pm 3$ μm of the HOM fiber tip with respect to the optimal focus point.

slope of the loss of a MOX to compensate for other sources of WDL in the DMD (fiber WDL, temperature dependent WDL).

2.3.4. Insertion and Return Losses Due to Surface Reflections and Scattering

The main source for return loss in the typical MOX architecture of Fig. 6 could be back-reflections at the fiber ends due to refractive index mismatch. Unless cleaved at an angle, each fiber end reflects about ~3.3% (=$[(1.444\text{-}1)/(1.444+1)]^2$) of the incident light, or –15 dB. Light hitting the fiber end from within the fiber (e.g., at the MOX input), returns with a tilted wavefront, whose overlap with the fiber backward propagating mode is very small (< -60 dB of return loss for an SMF with 8 degrees tilt). Conversely, light rays incident on the fiber tilted end face at the focus of a converging beam (e.g., following L2 in the upper part of Fig. 6), return into the focusing lens with angles outside the numerical aperture cone of a properly designed lens, again ensuring small back reflection. For both processes to succeed, the tilt angle must increase with the fiber numerical aperture (NA). For SMF fibers, the preferred angle is 8 degrees. Due to the larger NA (0.36–0.42) of the LP_{02} mode, to achieve back-reflection performance similar to that of SMF, tilt angles in excess of 16 degrees should be used, at the expense of unacceptable levels of polarization dependent loss (PDL). Angles around 10 degrees were adopted as a compromise, resulting in return loss values approaching –30 dB.

Tilting the fiber end faces will not prevent back-reflections from the free space optical elements in the MOX to contribute to its return loss performance. In the typical architecture shown in Fig. 6 there are an additional eight surfaces of optical elements. They must have high-quality antireflective coating and be properly aligned to ensure low insertion and reflection losses.

2.3.5. Temperature Effects

When the MOX is properly designed mechanically, temperature affects the system mainly through a defocus created at the fiber collimators. The following effects occur when the system is heated:

- Expansion of the lenses, leading to increase of the focal length.
- Change of the refractive index of the lenses, leading to either increase or decrease of the focal length, depending on the properties of the glass.
- Expansion of the metal holders of the collimators, which may compensate for the increase of the focal length.

These processes in combination cause an effective change of the focus position of the collimators, and may result in temperature dependent loss (TDL) and wavelength dependent loss (WDL). Athermal design of the MOX can be achieved by proper choice of materials for the lenses and metal holders, so that the different temperature effects will compensate one another. Deterioration of the quality of phase transformation due to a change in the refractive index and expansion of the phase elements is negligible when compared with the defocusing effect.

2.4. Actual Performance of the MOX

Experimentally, one usually characterizes a pair of MOXes, having a very short piece of HOM fiber between them. Such experimental data will be presented in Sections 4 and 5. However, to satisfy the inquisitive reader we conclude this section with the most important characteristics of manufactured MOXes:

- MOX insertion loss lies in the range of 0.8–1.25 dB.
- Wavelength dependent loss (WDL) can be minimized to below 0.1 dB over the C-band.
- Back reflection from the MOX below –28 dB.

- No PMD (a few fsec at most).
- Insignificant PDL if fiber angles do not exceed $\sim 10^\circ$.
- High power tolerance (no damage at 30 dBm).
- Size: a cylinder of diameter $\sim$1 cm and length of 6 cm.

Table 1. Maximum MOX extinction ratios over the C-Band for the three relevant modes. Best values refer to results obtained in a controlled laboratory environment, whereas typical values refer to volume production.

	Extinction ratio (dB)	
Mode	Best	Typical
LP_{01}	-26	-22
LP_{11}	< -30	-24
LP_{21}	< -35	< -30

As for individual extinction ratios, these were measured using a novel technique to be described in section 3.4.2.3, and the results are summarized in Table 1. Note that modes LP_{03} and LP_{12} can be easily removed using attenuation loops, see section 3.4.2.2, and therefore are of much less practical importance.

3. High-Order Mode Fibers for Dispersion Compensation

Having developed high-quality spatial mode transformers, it is our task now to show that HOM fibers (HOMF) can be designed to achieve the required dispersion properties (i.e., dispersion coefficient and dispersion slope coefficient), to compensate all modern transmission fibers, without sacrificing other importing properties, such as effective area. Combining the specially designed HOMF with the mode transformation technology of section 2, it has been possible to develop improved DCMs for use in modern high capacity optical transmission systems.

In this section we focus on the design and implementation of such HOMF. In section 3.1 we describe the selection criteria for the mode to be used for the purpose of dispersion compensation. In section 3.2 we discuss whether and how the mode transformation technology affects the design of the HOMF. In section 3.3 we discuss the required dispersion characteristics of the HOMF, while in section 3.4 we consider the design of the HOMF refractive index profile to achieve these characteristics. Finally, in section 3.5 we discuss the addition of a *trim* fiber to fine-tune the dispersion characteristics of the HOM-DCM.

3.1. Which High-Order Mode?

A key issue in the design of HOMF is which higher order mode the signal is to propagate in. Since our goal is dispersion compensation, one would naturally tend to choose the mode that gives the most desirable dispersion characteristics. However, it turns out that other design issues limit the choice of modes.

The most important amongst these issues is multi-path interference (MPI), which was mentioned in the introduction to this paper and will further be considered in section 4 below. Generally speaking, in order to limit MPI, one should limit the number of guided modes, and thus the possible interference paths in the HOMF. This means that the signal should propagate in the lowest order mode that still provides the required dispersion characteristics. For example, see Fig. 3, if we were to select the LP_{11} mode as the propagation mode, then it would be possible to design a fiber with only two guided modes (LP_{01}, LP_{11}). On the other hand, if we were to select the LP_{03} mode there would have to be at least six guided modes (LP_{01}, LP_{11}, LP_{02}, LP_{21}, LP_{12}, LP_{03}), and almost certainly some others as well. This means that even if the LP_{03} mode were to exhibit particularly attractive dispersion properties, the increased MPI due to MOX coupling to other modes would be very prohibitive.

A second important consideration is polarization dependent behavior, and particularly polarization mode dispersion (PMD). Modes that are not cylindrically symmetric are by their nature more susceptible to polarization effects, and thus may have much larger PMD than cylindrically symmetric modes. Since PMD is a key design issue for DCMs, this effectively restricts the selection of modes to those with cylindrical symmetry, i.e., $\mathrm{LP}_{\mathrm{on}}$.

The preceding discussion basically means that the LP_{02} mode is the logical choice for the propagation mode in HOMFs for HOM-DCMs. In fact, we will see that with proper fiber design this mode also provides the required dispersion properties for most applications, and is thus well suited for the task. Therefore, for the remainder of this paper we will consider only HOMFs where LP_{02} is the designated propagation mode.

3.2. Interdependence of MOX and Fiber

As discussed in section 2, for HOMF to be useful it needs to be accompanied by mode transformers (MOXes) at the input and output of the HOM-DCM. An important practical issue is whether and how the two basic components of the HOM-DCM, HOMF and MOXes, are interrelated, and how the design of each depends on the other. From the discussion of spatial mode transformation technology in section 2 it is clear that the mode transformers need to be designed specifically for a given HOMF. More importantly however, it was also shown that in principle the design methodology is powerful enough to handle almost *any* HOMF. This indicates that the two problems can be separated, i.e., the HOMF can be designed and implemented independently, and then the mode transformers may be designed in the second stage.

Nevertheless, there are still two issues related to spatial mode transformation that do influence the design of HOMF. The first is the necessity to keep the spatial distribution of the high-order mode relatively constant over the transmission band, so as to maintain low insertion loss and high extinction ratio of the MOXes for all wavelengths. Since wavelength-dependent steep changes in spatial distribution go hand in hand with steep changes in the effective index, which in turn means large dispersion, it would appear that high dispersion HOMF and spatial mode transformation may not well suite each other. However, it turns out that for dispersion values in the range of practical interest, about 200–600 ps/nm/km, the rate of change of the mode shape is still small enough to allow efficient and broadband spatial mode transformation (see section 2.1.4). A second, equally important issue is the necessity to design the HOMF such that the LP_{03} mode is as close to cutoff as possible, or preferably not guided at all. The reason for this is that typical spatial mode transformers only provide high extinction ratio between LP_{02} and LP_{03} at the center of the band, whereas towards the band edges the extinction ratio deteriorates sharply, see Fig. 8. This means that in order to maintain sufficiently low MPI across the band, it is necessary for the LP_{03} mode to be below or very close to cutoff (in the latter case special attenuation loops may be used to effectively kill the LP_{03} mode, see section 3.4.2.2)

3.3. Required Dispersion Characteristics of the HOMF

Clearly, the main requirement of a HOM-DCM is to provide accurate broadband dispersion compensation. Therefore, the most important characteristics of the HOMF are its dispersion characteristics, or more specifically the dispersion characteristics of the propagation mode of the HOMF, in our case, the LP_{02} mode. For the sake of brevity, we shall often use the term "dispersion of the HOMF" while actually meaning the dispersion of the LP_{02} mode of the HOMF

3.3.1. Simultaneous Slope and Dispersion Matching

To achieve linear distortionless transmission, the dispersion curve of the HOM-DCM should be a negative mirror of the dispersion curve of the transmission span to be compensated. Since the dispersion curve of all types of transmission fiber is very well approximated by a linear curve within a given transmission band, the dispersion curve of a transmission span of length L (in units of ps/nm) may be written as

$$D_{\rm span}(\lambda) = D(\lambda_0)\cdot L + S(\lambda_0)L(\lambda-\lambda_0) = D(\lambda_0)L\left(1+\frac{S(\lambda_0)}{D(\lambda_0)}(\lambda-\lambda_0)\right), \tag{14}$$

where λ_0 is some wavelength within the band (e.g., 1550 nm for the C-band), and $D(\lambda_0)$ and $S(\lambda_0)$ are the dispersion coefficient and dispersion slope coefficient of the transmission fiber at λ_0. Equation (14) shows that the dispersion curve may be characterized by: (1) The total dispersion given by $D_{\rm span} = D(\lambda_0)L$; (2) The ratio $S(\lambda_0)/D(\lambda_0)$, which does not depend on the length L, and therefore is a characteristic of the type of transmission fiber. This second quantity is often denoted as the RDS of the fiber [16], while the inverse quantity $D(\lambda_0)/S(\lambda_0)$ is denoted as κ [17]. Alternatively, an equivalent quantity can be defined, referred to as the Projected Zero Dispersion wavelength (PZD) [18],

$$\mathrm{PZD}\,(\lambda_0) = \lambda_0 - \frac{D(\lambda_0)}{S(\lambda_0)} = \lambda_0 - \frac{1}{\mathrm{RDS}} = \lambda_0 - \kappa. \tag{15}$$

The physical meaning of the PZD(λ_0), Fig. 18, is the wavelength for which the *linear approximation* of the fiber dispersion curve at wavelength λ_0 crosses the zero dispersion axis. An advantage of using the PZD is that for linear and quasi-linear dispersion curves the value of PZD does not depend on center wavelength λ_0, in contrast to κ and RDS. Table 2 enumerates the *dispersion properties* of common transmission fibers in the C and L bands.

Thus, to compensate the (assumingly linear) dispersion of a transmission fiber, having dispersion of $D_{\rm span}\,@\,\lambda_0$ and an RDS value $\mathrm{RDS}_{\rm TF}$, the HOMF needs to fulfill the following two conditions:

Table 2. Nominal Dispersion, Dispersion slope, RDS, κ and PZD for a number of common transmission fibers in the C and L bands. The dispersion is calculated at 1550 nm for the C-Band, and 1590 nm for the L-Band. eLEAF, Truewave and Teralight are trademarks of Corning, Inc., OFS Fitel L.L.C. Inc., and Alcatel Corporation, respectively.

Fiber type	Band	Dispersion (ps/nm/km)	Slope (ps/nm^2/km)	RDS (nm^{-1})	κ (nm)	PZD (nm)
SMF-28	C	17	0.057	0.0035	291	1261
	L	19	0.057	0.0030	331	1261
TrueWave-RS®	C	4.4	0.045	0.010	98	1452
	L	6.2	0.045	0.0072	138	1452
eLEAF®	C	4.2	0.087	0.020	49	1501
	L	7.6	0.087	0.011	89	1501
TeraLight®	C	8	0.057	0.071	140	1410
	L	10.3	0.057	0.0056	180	1410

$$\mathrm{RDS}_{\mathrm{HOMF}}\left(\lambda_0\right) = \mathrm{RDS}_{\mathrm{TF}}\left(\lambda_0\right), \tag{16}$$

$$D_{\mathrm{HOMF}}(\lambda_0) L_{\mathrm{HOMF}} = -D_{\mathrm{span}}(\lambda_0), \tag{17}$$

where $\mathrm{RDS}_{\mathrm{HOMF}}\left(\lambda_0\right)$ is the RDS of the HOMF at λ_0, $D_{\mathrm{HOMF}}\left(\lambda_0\right)$ is the dispersion coefficient, and L_{HOMF} is the length of the HOMF.

Clearly, the larger the absolute value of $D_{\mathrm{HOMF}}\left(\lambda_0\right)$, the less HOMF we need, which leads to a reduction in insertion loss of the HOM-DCM. In this context one can use the so-called Figure of Merit (FOM) introduced to characterize single mode DCF, and defined as the ratio of the fiber dispersion coefficient to the attenuation coefficient. The higher the FOM, the lower the resulting module loss of the DCM. For early DCFs, with dispersion in the range 90–120 ps/(nm km) and attenuation of 0.4–0.5 dB/km, The FOM was in the range of 200–300 ps/(nm km dB). Recent improvements in DCF design and manufacturing have led to FOM values nearing 500 [19].

For practical implementations of HOMF it is quite feasible to achieve dispersion values up to 600 ps/(nm km), with attenuation in the range 0.45–0.6 dB, resulting in FOM up to ~1000 ps/(nm km dB). While such high FOM potentially enables HOM-DCMs with very low module loss, one still has to account for the extra loss of the two MOXes, typically about 2 dB. This means that for DCMs compensating 80–100 km of transmission fiber, the high HOMF FOM does not translate into a significant improvement in module loss compared to state of the art DCF. However, for applications such as multi-span compensation (see section 5.3.1), where more negative dispersion fiber is required, the high HOMF FOM can be used to good advantage. The high HOMF FOM also results in savings in cost and packaging space.

3.3.2. Third-Order Dispersion (TOD)

While the dispersion curve of the transmission fiber can be considered linear, the HOMF dispersion curve quite often displays significant deviations from linearity within the transmission band. This nonlinearity of the dispersion curve is often referred to as third-order dispersion (TOD), or dispersion curvature, and is especially relevant when the dispersion coefficient and/or the dispersion slope coefficient have large negative values.

For a dispersion curve that deviates significantly from linearity over the transmission band, specifying the dispersion and RDS at λ_0 is only partially useful, and does not tell us anything about the overall behavior of the curve. Specifically, we would like to introduce an *average* RDS that represents the curve as a whole over the transmission band, and also introduce a measure for the deviation of the curve from linearity. To achieve both goals we introduce a linear fit to the dispersion curve such that *the maximum deviation of the actual curve from the linear fit within the transmission band* is minimized. This is different from the usual least mean squared (LMS) fit, since we aim to minimize the *maximum* deviation, and not the *average* deviation. An example of such a fit and the deviation from linearity is shown in Fig. 18.

Using the linear fit (LF), conditions (3.3) and (3.4) may be rewritten as

$$\mathrm{RDS}_{\mathrm{HOMF-LF}} = \mathrm{RDS}_{\mathrm{TF}}\left(\lambda_0\right), \tag{18}$$

$$L_{\mathrm{HOMF}} D_{\mathrm{HOMF-LF}}\left(\lambda_0\right) = -D_{\mathrm{span}}\left(\lambda_0\right)\ , \tag{19}$$

where $\mathrm{RDS}_{\mathrm{HOMF-LF}}$ and $D_{\mathrm{HOMF-LF}}\left(\lambda_0\right)$ refer to the linear fit. Then the residual dispersion (RD) of the transmission span + HOM-DCM is given by

$$\begin{aligned} \mathrm{RD}\left(\lambda\right) &= D_{\mathrm{span}}\left(\lambda\right) - L_{\mathrm{HOMF}} D_{\mathrm{HOMF}}\left(\lambda\right) \\ &= L_{\mathrm{HOMF}}\left[D_{\mathrm{HOMF-LF}}\left(\lambda\right) - D_{\mathrm{HOMF}}\left(\lambda\right)\right], \end{aligned} \tag{20}$$

where $\left[D_{\mathrm{HOMF-LF}}\left(\lambda\right) - D_{\mathrm{HOMF}}\left(\lambda\right)\right]$ is the deviation of the HOMF dispersion curve from linearity, as in Fig. 18. Since the objective is to minimize RD(λ) over the transmission band, i.e., to minimize $\max\limits_{\lambda \in \mathrm{Band}} RD\left(\lambda\right)$, the advantage of using this type of linear fit becomes clear: Any other linear fit would *by definition* lead to higher residual dispersion at some wavelength, whereas here the *maximum* residual dispersion is minimized over the whole transmission band. It also provides us with an important *measure* of the deviation from linearity. To make this measure independent of HOMF length, we may use Eqs (19) and (20) to write

$$\max_{\lambda \in \mathrm{Band}} RD\left(\lambda\right) = D_{\mathrm{span}}\left(\lambda_0\right) \frac{\max\limits_{\lambda \in \mathrm{Band}}\left[D_{\mathrm{HOMF-LF}}\left(\lambda\right) - D_{\mathrm{HOMF}}\left(\lambda\right)\right]}{D_{\mathrm{HOMF-LF}}\left(\lambda_0\right)}. \tag{21}$$

We now define the third order dispersion (TOD) of the HOMF as

$$TOD = 100\,\frac{\max\limits_{\lambda \in \mathrm{Band}}\left[D_{\mathrm{HOMF-LF}}\left(\lambda\right) - D_{\mathrm{HOMF}}\left(\lambda\right)\right]}{D_{\mathrm{HOMF-LF}}\left(\lambda_0\right)}, \tag{22}$$

i.e., the maximum deviation from the linear fit as a percentage of $D_{\mathrm{HOMF-LF}}\left(\lambda_0\right)$. Thus

$$\max_{\lambda \in \mathrm{Band}} RD\left(\lambda\right) = D_{\mathrm{span}}\left(\lambda_0\right) \mathrm{TOD}_{\mathrm{HOMF}}/100, \tag{23}$$

which means that TOD of the HOMF is a direct measure of the *maximum residual dispersion over the transmission band.*

To summarize, we may say the HOMF should ideally satisfy three conditions:

- Largest negative dispersion coefficient possible (to minimize HOMF length)
- Correct RDS as defined by Eq. (18) (broadband compensation).
- Smallest TOD possible (to minimize residual dispersion).

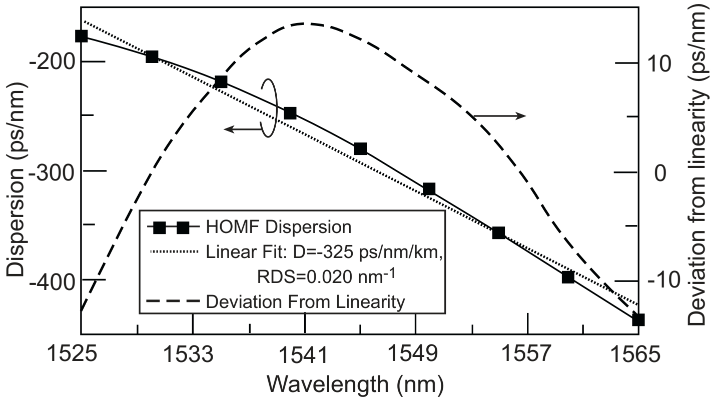

Fig. 18. Measured dispersion curve, linear fit, and the difference between the two (i.e. deviation from linearity) for a sample HOMF.

3.4. *HOMF Refractive Index Profile Design*

In this section we discuss the design of the refractive index profile of the HOMF. As a concrete example we concentrate on the compensation of Corning eLEAF® transmission fiber, which according to Table 2 has a high RDS value of 0.02 nm^{-1}. Such a high RDS is difficult to achieve using conventional DCF without resorting to very low effective area (typically about 15 μm^2 [20], highlighting the advantage of HOM-DCMs. It should be stressed, however, that the design principles discussed below equally apply to HOMF for any type of transmission fiber.

3.4.1. Basic Three Zone Profile and Dispersion Curve

The physics behind the three-zone profile used for DCF is well known within the context of single mode DCF, which is designed to have high negative dispersion in the basic LP_{01} mode. However, the same arguments apply just as well to higher order modes.

Figure 19 shows a typical three-zone profile of a HOMF used for dispersion compensation. The profile includes an inner core region with high relative refractive index (in this case $\Delta_1 = 1.47 - 1.444 = 0.026$), a depressed index region, and an outer core region. To understand the mechanism for the high negative dispersion of the LP_{02} mode, Fig. 20(a) shows the mode intensity distribution at 1550 and 1650 nm. As can be seen, the LP_{02} mode undergoes a sharp transformation from being mainly concentrated within the inner core region, to being mainly concentrated in the outer core region. This, and the accompanying change in effective index, leads to the sharp negative dispersion of the mode in this wavelength region, as clearly illustrated in Fig. 20(b).

Figure 21 shows a zoom-in of the dispersion curve to the region of interest for dispersion compensation. The general shape is shown in Fig. 21(a), and is common

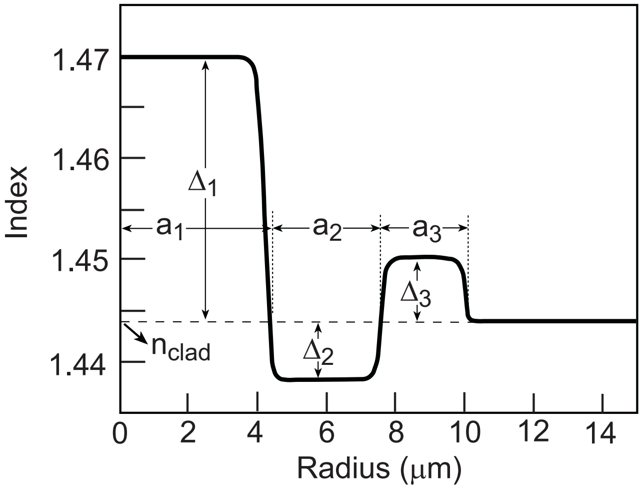

Fig. 19. Typical three zone profile of a HOMF for dispersion compensation. $\varDelta_1$, $\varDelta_3$ and $\varDelta_3$ are the relative (to the clad) indices of the zones, while a_1, a_2 and a_3 are the zone widths.

to all three-zone profiles of the type shown in Fig. 19 (and indeed to other profiles used for dispersion compensation). At shorter wavelengths the curve is concave, then passes through a zero-curvature point (in this case at about 1570 nm), after which it becomes convex and reaches a minima. By changing the various profile parameters, one can control the curve parameters, such as position along the wavelength axis, and the value of the minimum dispersion. Through such manipulations, to be discussed in more detail in section 3.4.3, one can achieve the desired dispersion characteristics within the transmission band of interest.

Figure 21(b) shows the dispersion curve in the C-band, together with a linear fit as described in section 3.3.2. On the basis of the linear fit, we see that the dispersion at 1550 nm is –376 ps/nm/km, and the RDS is 0.02 nm^{-1}. Thus, if we consider an 80-km eLEAF® span, we would need only 0.9 km of HOMF to achieve full dispersion and dispersion slope compensation of the span. These impressive dispersion characteristics have been achieved while maintaining a large mode effective area, which is 51 μm^2 at 1550 nm, and above 44 μm^2 over the entire C-band, as shown in Fig. 22. While recent single mode DCF designs have achieved comparable dispersion slope characteristics [20], the corresponding effective area is typically $\sim$15 μm^2, over three times smaller than the HOMF. Furthermore, the HOMF fiber profile itself is quite standard and easily manufactured. While the inner core index is high compared to standard SMF transmission fiber, it is comparable to regular DCF fiber, and can easily be achieved using standard manufacturing processes. The inner core radius is over 4 μm, much larger than DCF, and comparable to SMF, which further simplifies manufacturing. The measured dispersion curve of a fiber manufactured according to a profile similar to Fig. 19 is shown in Fig. 18, showing similar characteristics to the simulated curve.

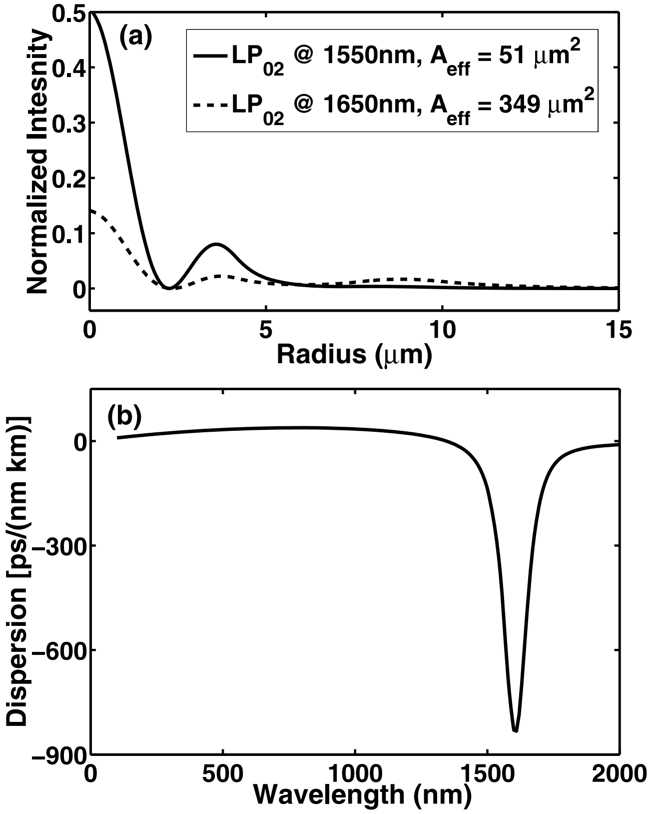

Fig. 20. (a) LP$_{02}$ mode intensity distribution at two different wavelengths, for the profile shown in Fig. 19. The effective area (A_{eff}) of the mode at the two wavelengths is given in the figure legends. (b) The associated *waveguide* dispersion curve (i.e., without material dispersion) showing the sharp transition in the region of the C-Band.

However, while the linear fit to the dispersion curve has ideal characteristics for dispersion compensation, the actual dispersion curve itself suffers from a non-negligible deviation from linearity, as is clearly visible from the curvature of the curve in Fig. 21(b). The corresponding TOD value, as defined in section 3.3.2, is 4.3%, meaning that for an 80-km span the resulting maximum residual dispersion after compensation will be about 15 ps/nm. For long haul links up to 1000 km this is probably not an issue, however, for ultra-long-haul links of 2000 km and above, the total accumulated residual dispersion will exceed 400 ps/nm, which is already sufficient to incur a non-negligible transmission penalty at 10 Gb/s.

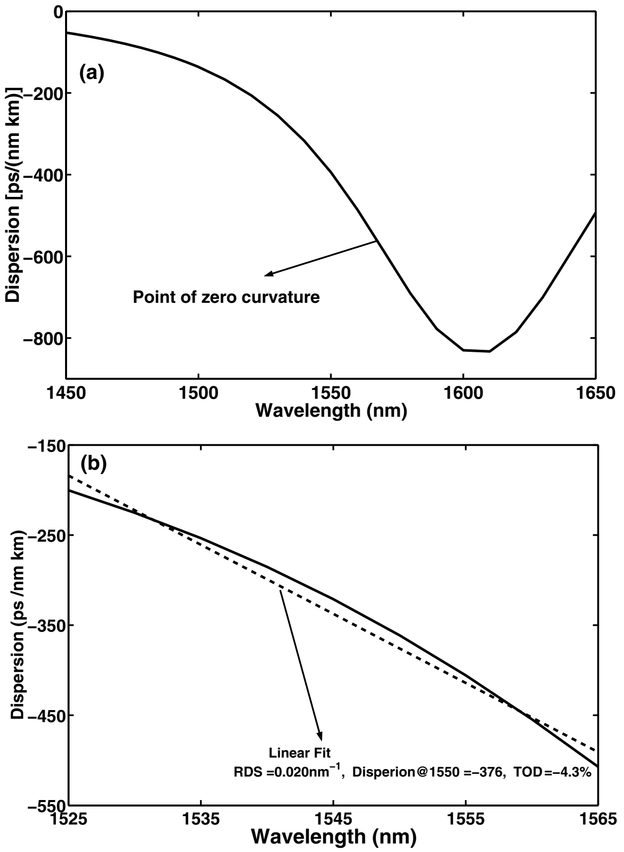

Fig. 21. Zoom-in of the LP_{02} mode dispersion for the profile shown in Fig. 19. (a) within the wavelength range 1450–1650. (b) within the C-band, together with the linear fit.

3.4.1.1. Relation Between TOD and RDS

Ideally, we would like to reduce the TOD while still maintaining the *RDS value* dictated by the transmission fiber to be compensated. While this is possible to some extent, it usually involves trade-offs with other important fiber properties, such as the n_{eff} of LP_{02} to be discussed in section 3.4.2 below. In practice, the TOD is strongly related to the RDS of the fiber, so that a meaningful reduction in TOD can only be achieved at the expense of reducing the RDS of the HOMF. This relation is to be expected, since higher RDS means higher dispersion slope (relative to dispersion), i.e., stronger dependence of the dispersion on wavelength. Since the dispersion curve is in any case strongly non-linear [Fig 21(a)], this results in higher TOD. In section 3.5 we will show that even if the RDS of the HOMF is not strictly the same as that of the transmission fiber, one can still obtain accurate broadband compensation using an additional trim

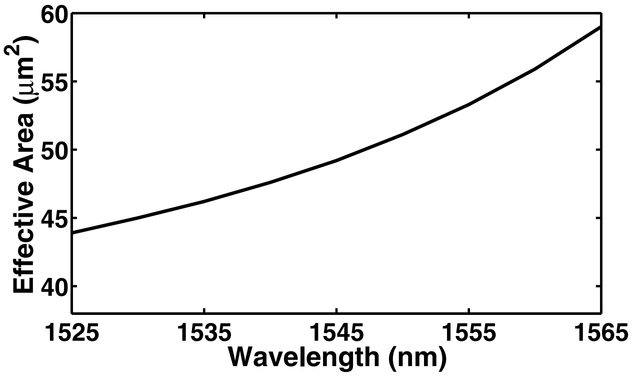

Fig. 22. Effective area as a function of wavelength for the profile of Fig. 19

fiber. This allows us some freedom in choosing the RDS of the HOMF in order to optimize other parameters, such as the TOD.

To illustrate this we have slightly altered the profile of Fig. 19 by decreasing the parameter a_2, the width of the 2nd profile zone, which as discussed in section 3.4.3.2 below, leads to a reduction in RDS. The resulting dispersion curves and deviation from linear fit for a reduction of 10% and 25% in a_2 are shown in Fig. 23, along with the original dispersion curve of Fig. 19. At an RDS value of 0.017 nm^{-1}, the TOD is reduced by more than half to 2.1%, whereas at an RDS value of 0.011 nm^{-1} it is reduced by an order of magnitude to 0.4%. The extremely low TOD in the latter case results directly from the fact that the zero curvature point of the dispersion curve occurs within the C-band near 1545 nm.

It is important to stress that the issue of TOD is not unique to HOM-DCF, but is also relevant to high RDS single mode DCF fiber. For example, Wandel and co-workers [20] present data for two high RDS DCFs. The first has RDS of 0.018 nm^{-1} and TOD above 5%, while the second has RDS of 0.01 nm^{-1}, and TOD of 0.4%. These reported TOD values are similar to those given in Fig. 23 for HOM-DCMs with comparible values of RDS.

Figure 23 also illustrates the relation between RDS and dispersion, or alternately between RDS and FOM. The lower the RDS, the easier it is to achieve high dispersion values, and thus high FOM values, while still maintaining other important profile characteristics discussed in the next section.

3.4.2. Other Important Characteristics of the Profile

The refractive index profile determines not only the dispersion characteristics, but also other properties of the HOMF, that can affect the performance of transmission systems. In this section we consider the more important of these properties, and how they are affected by the profile design.

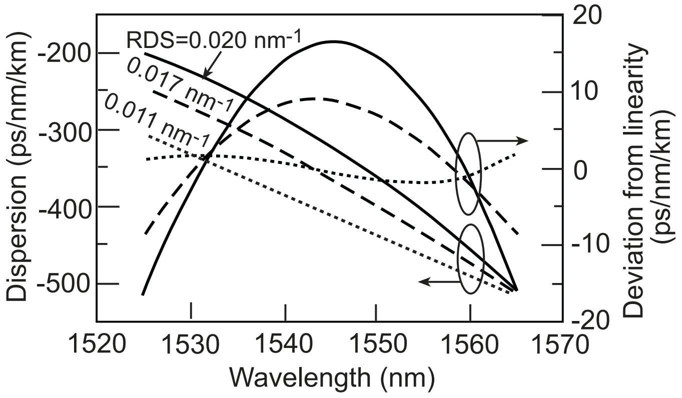

Fig. 23. Dispersion curves and deviation from linear fit for three different profiles: (a) Solid curves—The profile of Fig. 19, with linear fit parameters: RDS = 0.020 nm^{-1}, $D = -376$ ps/nm/km, TOD = 4.3%; (b) Dashed curves—The profile of Fig 19 with a_2 reduced by 10%, with linear fit parameters: RDS = 0.017 nm^{1}, $D = -405$ ps/nm/km, TOD = 2.1%; (c) Dotted curves—The profile of Fig 19 with a_2 reduced by 25%, with linear fit parameters: RDS = 0.011 nm^{-1}, $D = -429$ ps/nm/km, TOD = 0.4%.

3.4.2.1. Attenuation Coefficient and Effective Mode Cutoff

A mode is guided as long as its effective index is above the cladding index (typically 1.444 in the C-Band). Using this formal definition, the cutoff of the LP$_{02}$ mode of the profile of Fig. 19 is beyond 2000 nm. However, long before the formal cutoff is reached, the attenuation of the mode due to micro- and macro-bending [21] becomes so large as to render it unguided for all practical purposes.

One typically finds that the mode attenuation coefficient increases sharply when the effective index reaches a certain critical threshold, which depends on the fiber profile, the manufacturing process, and the fiber spooling conditions (which strongly affect micro-bending). The reason for this is that beyond this threshold, the mode extends away from the fiber core, and is more sensitive to various perturbations of the fiber profile, such as bending (both micro- and macro-).

The critical effective index in turn defines a critical wavelength, λ_c, which we call the *effective cutoff wavelength* of the mode (as opposed to the formal cutoff wavelength discussed above). In Fig. 24 we show the spectral dependence of the LP$_{02}$ attenuation coefficient of a fiber manufactured according to a profile similar to that of Fig. 19. One can clearly observe the onset of effective cutoff at about 1575 nm.

When designing the fiber profile, it is crucial to ensure that λ_c lies beyond the end of the transmission band. Since λ_c also depends on manufacturing conditions and on spooling, it is necessary to empirically determine the critical effective index for a given set of conditions. Once known, the profile may be designed so that the maximum effective index within the transmission band is above the critical effective index. We have determined that for a wide range of manufacturing and spooling conditions, the critical effective index for the LP$_{02}$ mode is in the range 1.4455–1.4460 (assuming

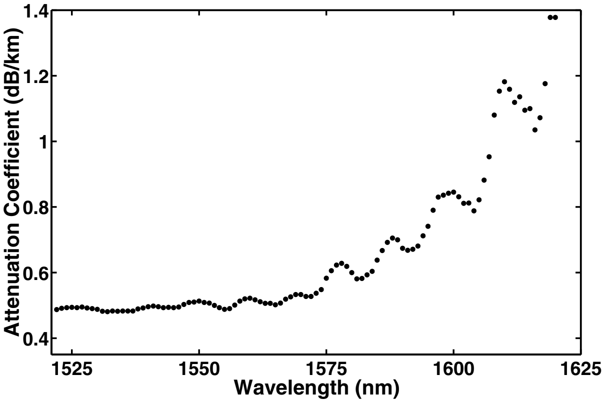

Fig. 24. LP_{02} attenuation coefficient of a fiber manufactured according to a profile similar to that of Fig. 19.

$n_{\text{clad}} = 1.444$). For the profile of Fig. 19 the effective index at 1565 nm is 1.4460, in accordance with the fact that λ_c lies beyond the C-Band (e.g., Fig. 24).

λ_c not only affects the mode attenuation coefficient, but also other fiber properties, notably polarization mode dispersion (PMD). Below λ_c, PMD has a weak spectral dependence, and is mainly determined by manufacturing and spooling conditions. Near λ_c, PMD takes on a stronger spectral dependence, and increases sharply beyond λ_c. The reason for this, as with the increase in attenuation, is that above λ_c the mode extends away from the fiber core, and becomes increasingly sensitive to perturations such as bending which break the fiber cylindrical symmetry. Practically speaking, the increased PMD means that even if the rise in attenuation due to effective cutoff can be tolerated, one should still design the profile to ensure that λ_c is beyond the transmission band.

Finally, Fig. 24 also illustrates the typical achievable attenuation coefficient for well-designed and manufactured HOMF, which is in the range 0.45–0.6 dB/km. This is similar to that of DCF with comparable dispersion characteristics [19].

3.4.2.2. Number of Guided Modes

As discussed in section 3.1, a major concern in the design of HOMF is the number of guided modes supported by the fiber, with more guided modes resulting in higher MPI of the HOM-DCM (All modes are excited, even if to a small extent, by the wave incident on the HOMF tip [see overlap integral of Eq. (7)]. If they are guided, they contribute to MPI, otherwise, they just represent tolerable loss). The profile of Fig. 19 supports six guided modes, whose effective indices in the C-Band are listed in Table 3. While the exact values can change, the number and order of modes as listed in the table is typical to most profiles.

In particular, the three modes more guided than the LP_{02} mode, i.e., LP_{01}, LP_{11}, and LP_{21}, are expected to be present in most HOMF profiles designed to use the LP_{02}

mode. Therefore, one should always account for the presence of these three modes, for example, in the context of mode coupling to be discussed in section 3.4.2.3.

On the other hand, there is some freedom regarding the two modes that are less guided than the LP_{02} mode, i.e., LP_{03} and LP_{12}. Using appropriate design, the effective indices of these modes may be decreased, and they may even be made to be non-guided, i.e., with effective indices below 1.4440. As discussed in section 3.2, this is particularly important with regards to LP_{03} due to MOX design issues. Even if the LP_{03} and LP_{12} modes are formally guided, i.e their effective index is above 1.4440, they may be strongly attenuated using special *attenuation loops* in the HOMF just after the input MOX, and just before the output MOX. These loops work on the principle that the macro-bending loss of a mode is strongly dependant on the effective index. For a step index fiber it has been shown that the macro-bending loss, α, associated with a loop of curvature radius R satisfies [22]

$$\alpha \propto \frac{1}{\sqrt{R}} \exp\left[-\frac{2}{3}\frac{(n_{\text{eff}} - n_{\text{clad}})^{3/2}}{n_{\text{eff}}^2} k \cdot R\right] \equiv \frac{1}{\sqrt{R}} \exp\left(-\frac{R}{R_c}\right), \tag{24}$$

where n_{clad} is the cladding index, and k the free space wavevector. Thus it is natural to define a critical radius R_c, such that loops with radius $R < R_c$ strongly attenuate the mode. In Table 3 we also list the critical radius for each mode at the beginning and end of the C-Band. This shows us that if we introduce attenuation loops of radius R $\sim$ 2cm, these loops should strongly attenuate the LP_{03} and LP_{21} mode, while only having a minor effect on the LP_{02} mode. Clearly, the smaller n_{eff} of LP_{03}, the easier it is to attenuate the mode. In practice we have found it desirable to keep the LP_{03} mode effective index below 1.4445 across the entire transmission band. Table 3 shows that the profile of Fig. 19 does not strictly satisfy this requirement. On the other handthe altered profile with RDS = 0.017 nm^{-1} (Fig. 23) does, with virtually no change to n_{eff} of the LP_{02} mode.

Table 3. Guided modes of the profile of Fig. 19, their effective indices, and critical bending radii [according to Eq. (24)].

	Effective index		Critical Bending radius R_c (mm)	
Mode	at 1525 nm	at 1565 nm	at 1525 nm	at 1565 nm
LP_{01}	1.4653	1.4651	0.3	0.3
LP_{11}	1.4582	1.4577	0.5	0.5
LP_{21}	1.4492	1.4484	2.0	2.6
LP_{02}	1.4467	1.4460	5.4	8.5
LP_{03}	1.4447	1.4445	41.0	67.9
LP_{12}	1.4446	1.4445	51.7	67.9

3.4.2.3. Mode Coupling

Mode coupling refers to transfer of optical power between modes propagating along the fiber. Power transferred from a guided mode to a non-guided mode results in loss, since the power in the non-guided mode dissipates along the fiber. However, power transferred to another guided mode continues to propagate, and at a later stage (either further along the HOMF, or at the output MOX) can recombine with the main signal and lead to MPI. The precise relation between mode coupling and MPI will be discussed in section 4.4.2, whereas here we discuss mode coupling in general, and how it is affected by the fiber profile design.

Mode coupling occurs due to random perturbations of the refractive index profile along the fiber. These may results from manufacturing imperfections, or external causes such as stress and micro-bending [21]. Since the perturbations are random, the mode coupling is *incoherent*, as opposed to coherent mode coupling that occurs due to a systematic perturbation along the fiber (e.g., Bragg gratings). Thus, the power transfer rate between modes is constant, and independent of position along the fiber, allowing one to define a mode-coupling coefficient between any two modes denoting the power transfer rate. For example, a mode coupling coefficient of 0.01 km^{-1} between the LP_{02} mode and the LP_{01} mode means that every km, 1% of the LP_{02} power is transferred to the LP_{21} mode, and *vice versa*.

A detailed discussion of the mode-coupling coefficient is beyond the scope of this paper, and can be found, for example, in [23–25]. Furthermore, the details of any theory depend strongly on the types of perturbations and their statistics, data that is very difficult to extract experimentally from a fiber. Having said that, there are a few general observations that can be made about the factors that determine the mode-coupling coefficients:

- A given type of perturbation will have a specific symmetry, and thus only couple between certain modes [23]. For example, micro-bending will only couple between modes whose azimuthal numbers (m in the LP_{mn} notation) differ by unity, such as LP_{02} and LP_{11}, but not modes with the same azimuthal symmetry, such as LP_{02} and LP_{01}. Similarly, elliptic perturbations (i.e., perturbations that distort the cylindrical symmetry of the fiber), will couple between LP_{02} and LP_{21}, but again not between modes with the same azimuthal symmetry. For a given set of manufacturing and spooling conditions one typically finds that there are one or two dominant perturbations, and these determine the modes that couple most strongly to each other.
- As a general rule, the larger the difference in propagation constants of two modes $[\varDelta\beta = \beta_1 - \beta_2 = k(n_{\text{eff},1} - n_{\text{eff},2})]$, the smaller the mode coupling between them. However, the decrease in mode coupling occurs only for $\varDelta\beta$ larger than the inverse of the typical length scale of the perturbation causing the coupling. For smaller $\varDelta\beta$, the dependence on $\varDelta\beta$ is weak, since the perturbation length scale is in any case much smaller than the phase walk-off (i.e., $\varDelta\beta^{-1}$) between the two modes.
- Fibers whose profiles exhibit sharp features are more sensitive to perturbations along the fiber, and have higher mode coupling coefficients. Quantitatively, this is related to the profile derivative dn/dr, r being the radial coordinate. Referring to Fig. 19, it is clear that the larger the value of $\varDelta_1$, the sharper the transition between the first and second zones of the profile, and the larger is dn/dr at the boundary between two zones. The same applies to the magnitude of $\varDelta_2$ and $\varDelta_3$. However, since $\varDelta_1$ is typically much larger, it usually has the dominant effect. Thus, an important conclusion is that the higher $\varDelta_1$, the stronger the mode coupling.

In order to measure the mode-coupling coefficient we use a high resolution reflectometer [26] in a setup shown schematically in the left-hand side of Fig. 25. The output pulse of the reflectometer enters the MOX via the circulator and is then transformed primarily to the LP_{02} mode of the HOMF. As the pulse propagates along the HOMF, part of it is coupled to other modes, having different group velocities. The entire signal is then coupled from the HOMF back to an SMF fiber using a splice with a known lateral offset, and then, via the circulator back into the reflectometer. The lateral offset of the splice is necessary so that optical power carried by the LP_{11} and LP_{21} modes of the HOMF couples to the SMF and is thus able to reach the reflectometer. A sample reflectometer trace is shown in the right-hand side of Fig. 25, and consists of discrete peaks in between which there is a continuous signal. The discrete peaks correspond to power coupled to the different modes by the input MOX, and can be identified by comparing their position to the simulated group velocity of the fiber modes. As should be expected, the strongest peak corresponds to the LP_{02} mode. The continuum between the peaks represents power that was coupled from the LP_{02} mode to other modes at various points along the fiber.

Referring to Fig. 25 as an example, one can observe the following:

– The continuum between the LP_{01} peak and the LP_{02} peak is due to coupling from LP_{02} to LP_{01}.
– The continuum between the LP_{02} peak and the LP_{11} is due to coupling from LP_{02} to both LP_{11} and LP_{21}
– The continuum between the LP_{11} peak and the LP_{21} peak is due to coupling from LP_{02} to LP_{21}

By integrating these three continuums, comparing to the integrated LP_{02} power, and correcting for the HOMF-SMF coupling for each mode due to the lateral splice offset (these correction factors were calculated and verified experimentally), it is possible to derive the mode coupling coefficients between the LP_{02} mode and the three other modes. A variation of this technique can also be also used to derive the MOX extinction ratios, as for example listed in Table 1.

As discussed in the previous section, at least three other modes besides the LP_{02} mode are present in a typical HOMF: LP_{01}, LP_{11}, and LP_{21}. Thus, the three most important coupling coefficients for the design of HOMFs are between the LP_{02} mode and these three modes. We have measured these coupling coefficients for a wide range of fibers manufactured under different conditions, and have found the general behavior shown in Table 4. Thus, the LP_{02} – LP_{21} coupling is one to two orders of magnitude stronger than the LP_{02} – LP_{01} coupling, with LP_{02} – LP_{11} coupling somewhere in the middle. This order also corresponds to the decreasing order of Δn_{eff} (i.e., of $\Delta\beta$), as discussed above. However, caution should be exercised in concluding that $\Delta\beta$ has a critical impact on mode coupling, since the three types of coupling correspond to different perturbation symmetries. Thus, it is quite possible that a certain type of perturbation is dominant in the fibers, e.g., elliptical perturbations, and this is the main factor determining the order of the coupling strengths. In fact, for a given type of coupling, e.g., LP_{02}–LP_{21}, we have found no correlation between $\Delta\beta$ and the coupling strength, thus lending support to this possibility.

A key question remains as to which profile parameters affect the mode coupling strength. This is particularly relevant to LP_{02}–LP_{21} coupling, which is by far the dominant mechanism. As discussed above, one would expect the core relative index Δ_1 to influence the coupling strength, since higher Δ_1 leads to higher profile derivatives at

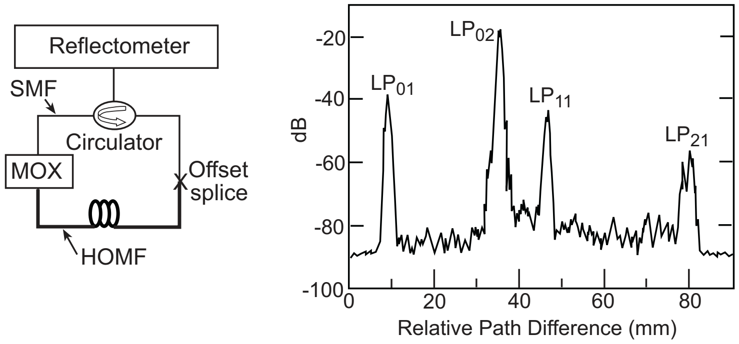

Fig. 25. Schematic representation of the mode coupling measurement setup (left), and sample output trace of the Reflectometer (right).

the boundary between the first and second profile zones. This is indeed apparent from Fig. 26, which shows the measured LP_{02}–LP_{21} coupling coefficient for a number of fibers having different values of Δ_1. Besides the issue of profile derivatives, it is well known that high levels of Germanium doping lead to increased Rayleigh scattering in fibers, and a similar mechanism may also be responsible for increasing the mode coupling (over and above the increase due to higher profile derivatives).

Table 4. Typical range of measured coupling coefficients between the LP_{02} mode and three other modes.

Between modes	Typical value of Δn_{eff}	Coupling coefficient (km^{-1})	
		Range	Typical
$LP_{02} - LP_{01}$	0.019	0.0001 – 0.001	0.0002
$LP_{02} - LP_{11}$	0.012	0.001 – 0.005	0.002
$LP_{02} - LP_{21}$	0.003	0.005 – 0.02	0.007

3.4.3. Profile Design Degrees of Freedom

The preceding sections presented the basic three-zone profile of the HOMF, together with the dispersion curve and other fiber properties. Here we consider the main degrees of freedom that allow one to control these properties.

3.4.3.1. Controlling the Dispersion Through Profile Scaling

As with the simple step index fiber [27] a scaling relation exists between the dimensions of the fiber profile and the wavelength. Specifically, scaling the fiber radius by a factor α (i.e., the parameters a_1, a_2 and a_3 in Fig. 19 are multiplied by α), results in a change in waveguide dispersion according to

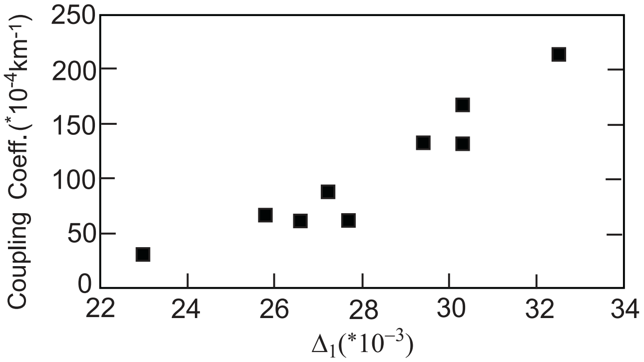

Fig. 26. Correlation between measured LP$_{02}$-LP$_{21}$ coupling coefficient and the core relative index Δ_1.

$$\tilde{D}_{\mathrm{WG}}(\lambda) = \frac{1}{\alpha} D_{\mathrm{WG}}\left(\frac{\lambda}{\alpha}\right). \tag{25}$$

Here $\tilde{D}_{\mathrm{WG}}(\lambda)$ is the waveguide dispersion of the scaled fiber, whereas $D_{\mathrm{WG}}(\lambda)$ is that of the original fiber. Equation (25) is easily derived from the wave equation of the fiber and the definition of waveguide dispersion. The total dispersion, including also material dispersion, does not strictly satisfy Eq. (25), however, for the high dispersion fibers discussed here, waveguide dispersion is by far the dominant contribution. The physical meaning of Eq. (25) is that scaling the fiber radius shifts the dispersion curve on the wavelength axis, as illustrated in Fig. 27 for the profile of Fig. 19. Thus, contracting/expanding the profile shifts the dispersion curve to shorter/longer wavelengths, having the effect of changing the dispersion at a given wavelength. For example, Fig. 27 shows that the dispersion at 1550 nm changes from –200 ps/nm/km to –750 ps/nm/km for a scaling range of only 4%.

Besides being an important design tool for achieving the required dispersion at a given wavelength, scaling also has an important practical aspect: When drawing a fiber during manufacturing, the outer diameter of the fiber, as well as all other transverse dimensions, may be altered by altering the drawing conditions. This results in scaling of the fiber profile, and allows fine-tuning of the dispersion during manufacturing.

3.4.3.2. Controlling the RDS

A given dispersion curve is characterized by the value of the dispersion and dispersion slope at each point along the curve. Scaling the profile shifts the dispersion curve along the wavelength axis, thus changing the dispersion for a given wavelength. However, for each value of dispersion, the slope, and hence the RDS, is predetermined by the shape of the curve. Thus, to achieve a different RDS for the same dispersion, the dispersion curve should be *altered*, as opposed to just shifting it along the wavelength axis. This basically means altering the depth of the dispersion minima, which can be achieved by changing the parameters of the second profile zone, i.e., the depressed index region.

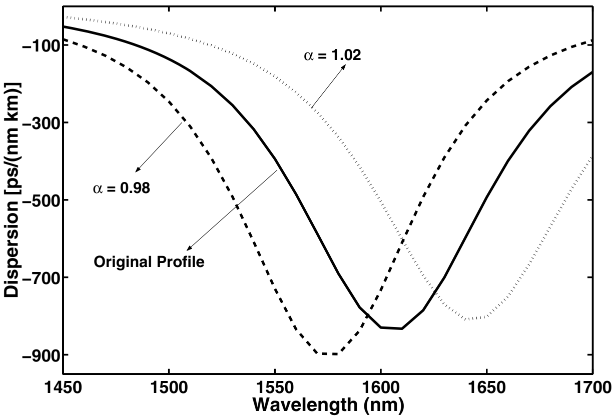

Fig. 27. The effect of the fiber scaling on the dispersion curve. The dispersion curve of the profile of Fig. 19 is displayed together with dispersion curves of the same profile where the radius is multiplied by a factor α.

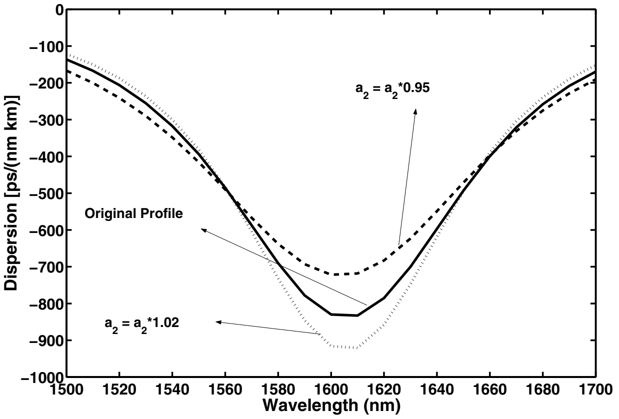

Fig. 28. The effect of a_2, the width of the second profile zone, on the dispersion curve. The dispersion curve of the profile of Fig. 19 is displayed together with dispersion curves for the same profile where a_2 is decreased by 5% and increased by 2%.

The deeper or wider this region, the deeper the dispersion minimum, and *vice versa*. Figure 28 shows the effect of a_2, the width of the second profile zone, on the dispersion curve, while a similar effect can be achieved by changing Δ_2, the depth of the zone.

The deeper the dispersion curve, the higher the achievable slope for a given dispersion, and the higher the RDS. For example, scaling the three curves shown in Fig. 28 to the same dispersion, results in RDS values from 0.017 nm^{-1} for the shallowest curve, to 0.022 nm^{-1} for the deepest curve. Another example can be seen in Fig. 23, where a reduction in a_2 leads to a significant decrease in RDS, with only minor change in the dispersion.

3.4.3.3. *Controlling the Mode Effective Indices*

As discussed in section 3.4.2.1, it is crucial to maintain high n_{eff} of LP_{02} in order to avoid effective cutoff occurring within the transmission band. In the previous two sections we saw how to modify the profile to achieve the desired dispersion and RDS. However, these modifications also alter n_{eff} of LP_{02}, with higher dispersion and RDS usually meaning lower n_{eff}. Thus, we would like to independently control n_{eff} so as to satisfy all three requirements simultaneously. This can be achieved through the core relative refractive index $\varDelta_1$: The higher $\varDelta_1$, the higher n_{eff} of all modes, including LP_{02}. This is easily understood since n_{eff} is nothing but a form of weighted average of the refractive index profile [27]. Increasing $\varDelta_1$ not only increases n_{eff}, but also changes the dispersion and RDS, which can then be altered using the methods of the previous sections. The important point is that we may achieve the same dispersion and RDS, but with a higher n_{eff} for the LP_{02} mode, thus providing independent control of the three parameters.

However, there are two problems with this approach: Fig. 26 shows that increasing $\varDelta_1$ above 0.28 leads to prohibitively high mode coupling (see also section 4.4.2), and should therefore be avoided. This limit on $\varDelta_1$ effectively limits the range of dispersion and RDS that may be achieved while still maintaining acceptably high n_{eff}.

The second problem is that n_{eff} of LP_{03} mode also increases with $\varDelta_1$. To overcome this we take advantage of the different intensity distributions of the two modes, as shown in Fig. 29. We see that most of the LP_{02} mode power is concentrated in the first and second profile zones, whereas most of the LP_{03} mode power is concentrated in the third profile zone. This allows us to achieve a degree of independent control of the n_{eff} of the two modes. For example, the relative index of the third zone, $\varDelta_3$, has a much larger impact on the n_{eff} of the LP_{03} mode than on that of the LP_{02} mode. Thus, by decreasing $\varDelta_3$ and then slightly increasing$\varDelta_1$, one can achieve the net effect of decreasing n_{eff} of LP_{03} while maintaining the n_{eff} of LP_{02}.

3.5. *Trim Fiber and HOM-DCM Design Options*

Up till now we have implicitly assumed that the only fiber within the HOM-DCM is the HOMF. Thus, the target dispersion and RDS of the HOMF are dictated by those of the HOM-DCM itself, as discussed in section 3.3. However, it has been noted before in the context of single mode DCF [28], that for applications where broadband dispersion compensation is critical, i.e., when it is necessary to simultaneously and accurately compensate for both slope and dispersion, it can be advantageous to use an additional fiber within the HOM-DCM, which we refer to as *trim* fiber. One of the advantages of trim fibers has to do with manufacturing tolerances. Naturally, it is impossible to manufacture HOMF exactly according to design specifications, and therefore it is necessary to specify manufacturing tolerances, namely, a range of dispersion and RDS values around the nominal design values. Any deviation of the actual dispersion coefficient from the design value may easily be compensated for by altering the length of the HOMF used in the HOM-DCM. However, deviations of the actual RDS from

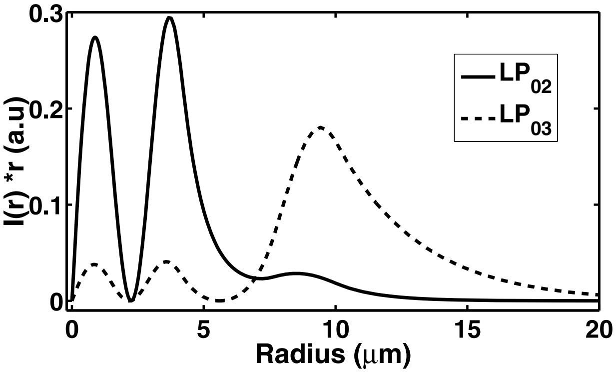

Fig. 29. $I(r) \cdot r$ corresponding to the LP_{02} and LP_{03} modes of the profile of Fig. 19 at 1550 nm, $I(r)$ being the modal intensity distribution.

the design value cannot be compensated for, and this results in a HOM-DCM with inaccurate dispersion properties. A trim fiber allows one to fine-tune the dispersion properties of the DCM to achieve accurate dispersion and RDS simultaneously.

Given the dispersion and dispersion slope coefficients of the HOMF, $D_{\mathrm{HOMF}}(\lambda_0)$ and S_{HOMF}, and the dispersion and dispersion slope coefficients of the trim fiber, $D_{\mathrm{Trim}}(\lambda_0)$ and S_{Trim}, it is easy to show that the lengths of HOMF and trim fiber required to achieve accurate dispersion compensation must satisfy the following equations:

$$D_{\mathrm{HOMF}}\left(\lambda_0\right) L_{\mathrm{HOMF}} + D_{\mathrm{Trim}}\left(\lambda_0\right) L_{\mathrm{Trim}} = D_{\mathrm{span}}\left(\lambda_0\right), \tag{26}$$

$$S_{\mathrm{HOMF}} L_{\mathrm{HOMF}} + S_{\mathrm{Trim}} L_{\mathrm{Trim}} = S_{\mathrm{span}}. \tag{27}$$

Note that the dispersion slope coefficients referred to in Eq. (27) are defined in the same manner as described in section 3.3.2, i.e., they do not represent the actual slope at λ_0, but rather the slope of the linear fit to the dispersion curves. Clearly, in order for Eqs. (26) and (27) to have physically meaningful solutions, i.e., for L_{HOMF} and L_{Trim} to both be positive, the dispersion characteristics of the trim fiber and HOMF must satisfy certain conditions. This just means that only certain types of trim fiber may be used in conjunction with given HOMF.

A good example for the use of trim fiber concerns HOM-DCMs designed to compensate eLEAF® transmission fiber, which has an RDS value of 0.020 nm^{-1}. If we design the RDS of the HOMF to be less than 0.020 nm^{-1}, say 0.018 $\mathrm{nm}^{-1}$with a manufacturing tolerance of $\pm$0.002 nm^{-1}, then it is easy to show that regular SMF fiber may be used as a trim fiber. The closer the RDS of the HOMF is to 0.020 nm^{-1}, the less trim fiber is required to achieve accurate dispersion compensation. However, even if the RDS of the HOMF is at the other end of the manufacturing tolerance range, i.e., 0.061 nm^{-1}, it is still possible to achieve accurate compensation by using the correct amount of trim fiber according to Eqs. (25) and (26).

Besides allowing relaxed manufacturing tolerances for the HOMF, trim fiber also allows additional freedom in the actual *design* of the HOMF. The main motivation for this is that even if we are able to manufacture HOMF with RDS close to that required, there is still the issue of TOD. Considering the example of a HOM-DCM for eLEAF® transmission fiber: we saw in section 3.4.1.1 that by reducing the RDS of the HOMF, we may significantly reduce the TOD as well. Thus, it may be desirable to purposely design the HOMF with lower RDS, relying on the SMF trim fiber to accurately provide the required dispersion compensation. This entails now a new trade-off, this time between TOD and the insertion loss of the HOM-DCM. The higher the RDS of the HOMF, the higher the TOD, but the less trim fiber needed, meaning less insertion loss. Conversely, the lower the RDS of the HOMF, the lower the TOD, but the more trim fiber is needed, increasing the insertion loss. To illustrate this trade-off, Table 5 shows three different design options for a C-band HOM-DCM for 80 km of eLEAF® transmission fiber, based on the three HOMF designs corresponding to Fig. 23. To calculate the insertion loss, we have assumed that each MOX contributes 1.25 dB, the attenuation coefficient of the HOMF is 0.5 dB/km, and the attenuation coefficient of the SMF fiber is 0.22 dB/km, all at 1550 nm. The module maximum residual dispersion is given by Eq. (23), and is the maximum residual dispersion over the C-Band of the HOM-DCM + transmission fiber.

Of the three options, option C is not particularly realistic from a packaging point of view, due to the large amount of trim fiber required. This just illustrates that while trim fiber allows us some freedom in choosing the RDS of the HOMF, it is still highly desirable to be as close to the target transmission fiber RDS as possible. The choice between options A and B (or similar ones), depends on the type of application being considered. For example, in links below 1000 km the accumulated residual dispersion for option A is less than 200 ps/nm, which is easily tolerated. Thus, the reduced insertion loss of the HOM-DCM for option A may be used to simplify the link design and reduce costs. Conversely, for links above 2000 km the accumulated residual of option A may be prohibitive, thus making option B more favorable.

Table 5. Different design options for a HOM-DCM for 80 km of eLEAF® transmission fiber, based on the three HOMF designs corresponding to Fig. 23.

Parameter	Option A	Option B	Option C
HOMF Dispersion (ps/nm/km)	−375	−405	−430
HOMF RDS (nm^{-1})	0.020	0.017	0.011
HOMF TOD (%)	4.3	2.1	0.4
HOMF Length (km)	0.9	1.1	1.7
SMF trim fiber length (km)	0	5.6	24.1
Maximum Residual Dispersion (ps/nm)	15	9	3
Module Insertion loss (dB)	2.9	4.3	8.7

3.6. *Summary*

In this section we have discussed the requirements for HOMF to be used in HOM-DCMs, and how to design refractive index profiles to meet these requirements. Using these design methods it is possible to achieve the high negative dispersion and dispersion slope necessary to compensate for most transmission fibers, without paying the price of a small effective area. Furthermore, it is possible to ensure that the LP_{02} mode is well guided, with attenuation of the same order as regular DCF, about 0.5 dB/km, while at the same time keeping mode coupling and the number of unwanted modes, and hence MPI (see section 4 below), at acceptable levels. Finally, we have shown how the addition of a trim fiber to the HOM-DCM allows us to fine-tune the dispersion characteristics, as well as providing additional freedom in the design of the HOMF (which can be used to reduce the TOD).

4. Multi-Path Interference (MPI)

While HOM-DCMs have much to offer in terms of dispersion characteristics, low insertion loss, and low non-linear effects, multi-path interference (MPI) remains a major concern that must be addressed. In this section we characterize MPI in HOM-DCMs, and discuss the system level impact of the effect.

4.1. Introduction

MPI refers to the interference of an optical signal with a replica of itself (which we will call a “satellite signal”) that has traversed a different path in the system. The classical example of MPI is multiple back reflections that create delayed replicas of the signal [29]. Such back reflections may be due to discontinuities in the systems (e.g. connectors and splices), or continuous Rayleigh backscattering, which is particularly relevant in system employing Raman amplification [30]. In HOM-DCMs, MPI results directly from the existence of additional modes within the HOMF besides the signal LP_{02} mode. A satellite is created when a portion of the signal couples to one of the additional modes, and then couples back to the main signal at a later stage. Such coupling can either occur within the MOXes, or along the HOMF itself due to mode coupling, as shown schematically in Fig. 30.

In general one can differentiate between two types of satellites, to be discussed in more detail in section 4.4: A *discrete* satellite is created when the coupling to the additional mode occurs at the input MOX, and the coupling back to the signal occurs at the output MOX. We use the term discrete since only one such satellite can exist for each mode within the HOMF, and both coupling events occur at distinct discrete points within the HOM-DCM. Conversely, mode coupling in the HOMF give rise to a *continuum* of small satellites, since coupling can occur at any point along the fiber (similar to Rayleigh scattering). In section 4.4 we show that due to the high efficiency of current MOX technology, discrete satellites make a relatively minor contribution to the total MPI. This means that the significant part of MPI in HOM-DCMs consists of a continuum of small satellites, which as we shall see below has important practical implications.

4.2. Definition of MPI

Consider a CW field input to a HOM-DCM exhibiting MPI. At the output of the system the optical field may be written as

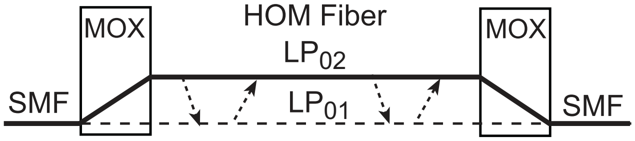

Fig. 30. Illustration of coupling between the main signal and an additional mode (e.g., LP_{01}). This coupling can occur within the MOXes, or along the HOMF.

$$\mathbf{E}(t) \propto \sqrt{P_0}\Bigg[\mathbf{p}_s \exp\left[j(\omega t + \varphi(t))\right] + \sum_i \mathbf{p}_i \sqrt{\varepsilon_i} \exp\left[j(\omega t + \varphi(t - \Delta\tau_i) + \Delta\psi_i(t))\right]\Bigg], \tag{28}$$

where P_0 is the average optical power, ω is optical frequency, $\mathbf{p}_s$ is the polarization of the main signal, $\varphi(t)$ represents laser phase noise, and $\mathbf{p}_i$, ε_i, $\Delta\tau_i$, $\Delta\psi_i(t)$ are respectively, the polarization, relative power, accumulated group delay difference and accumulated phase difference of satellite i. The summation is over all satellites created in the module, and in the case of a continuous source of MPI, should be replaced with an appropriate integral.

The optical power (averaged over a few optical cycles) detected at the output is then given by

$$P(t) = P_0\left[1 + 2\sum_i \sqrt{\varepsilon_i} \cos\left[\Delta\theta_i(t)\right] \cos\left[\varphi(t) - \varphi(t - \Delta\tau_i) - \Delta\psi_i(t)\right]\right], \tag{29}$$

where $\Delta\theta_i(t)$ is the relative angle between $\mathbf{p}_s$ and $\mathbf{p}_i$, and we have kept only the interference terms between the signal and the satellites, ignoring second order interactions. While $\Delta\theta_i(t)$ and $\Delta\psi_i(t)$ have relatively slow environmentally-governed time scales, the dynamics of $\varphi(t) - \varphi(t - \Delta\tau_i)$ are determined by the laser linewidth (a few MHz). The interference terms cause the power to fluctuate over time, with a standard deviation (over an infinitely long time) given by [31]

$$\sigma^2 = P_0^2 \sum_i \varepsilon_i, \tag{30}$$

where we have assumed no temporal correlation between the various satellites. Since the system impact of MPI is directly related to the standard deviation of power fluctuations, a convenient and useful definition of MPI is just sum of the satellite relative powers,

$$\mathrm{MPI} \equiv \sum_i \varepsilon_i. \tag{31}$$

The probability distribution function (PDF) of the power fluctuations approaches a Gaussian form as the number of satellites increases [31]. This has important implications for the system impact of MPI, and as we shall see further on, is the relevant case for MPI in HOM-DCMs.

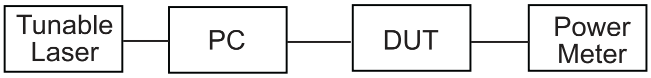

Fig. 31. MPI measurement setup. PC = Polarization controller, DUT = Device Under Test.

4.3. Measurement of MPI

In order to fully characterize the MPI of a device or system, it is necessary to have a standardized and reproducible measurement method. Referring to Eqs. (29)–(31), it is clear that by generating a full sample of phases $\{\Delta\psi_i(t)\}$ and polarization fluctuations$\{\Delta\theta_i(t)\}$, and measuring the resulting standard deviation of the output power fluctuations, one can directly measure the MPI.

To implement this we use the wavelength scanning method, also described in [32]. The measurement setup simply consists of a high coherence tunable laser [typically an external cavity laser (ECL), with a linewidth of a few kHz and $\sim$1pm spectral resolution], a polarization controller, and a power meter, as shown in Fig. 31. The method involves measuring the power for a range of wavelengths and polarization states, and calculating the average P_{avg} and standard deviation σ of the resulting measurement sample. From Eqs. (30 and (31), the MPI is then given by

$$\mathrm{MPI} = \frac{\sigma^2}{P_{\mathrm{avg}}^2}. \tag{32}$$

To gain further insight into this method we note that due to the use of a highly coherent laser, the laser phase noise difference $\Delta\varphi\,(\Delta\tau) \equiv \varphi(t) - \varphi(t - \Delta\tau)$ is identically zero. Thus, for a given wavelength and polarization state, the power remains constant over a long time (typically longer than 1 s), and can be accurately measured by a power meter with a long integration time. When the wavelength is changed, the path phase differences $\Delta\psi_i$ appearing in Eq. (28) changes in the following manner:

$$\Delta\psi_i\,(\lambda + \delta\lambda) = \Delta\psi_i(\lambda) + \frac{d}{d\lambda}\left[\frac{2\pi}{\lambda}\Delta L_{\mathrm{opt},i}\right]\delta\lambda = \Delta\psi_i(\lambda) + \frac{2\pi c\Delta\tau_i}{\lambda^2}\delta\lambda, \tag{33}$$

where c is the vacuum speed of light, and $\Delta L_{\mathrm{opt},i}$ and $\Delta\tau_i$ are, respectively, the optical path difference and group delay difference between satellite i and the signal. As long as $\Delta\tau_i > 1$ ns, which is the relevant case for HOM-DCMs (see Table 6 below), the quantity $c\Delta\tau_i/\lambda^2$ is larger than 0.1 pm^{-1}. Thus, by changing the wavelength by more than 10 pm we induce a phase difference larger than 2π, and effectively randomize the phase. By scanning a few hundred wavelengths within a narrow 1nm widow we can therefore generate a large random sample of phases for the various satellites. Similarly, by scanning a number of polarization states, the polarization angles $\Delta\theta_i$ may also be sampled, thus creating a representative sample of power fluctuations.

The wavelength scanning method can efficiently be implemented using a swept wavelength system that allows one to rapidly scan the entire C-band with a 1-pm resolution, and a number of different input polarization states. Then, by separating

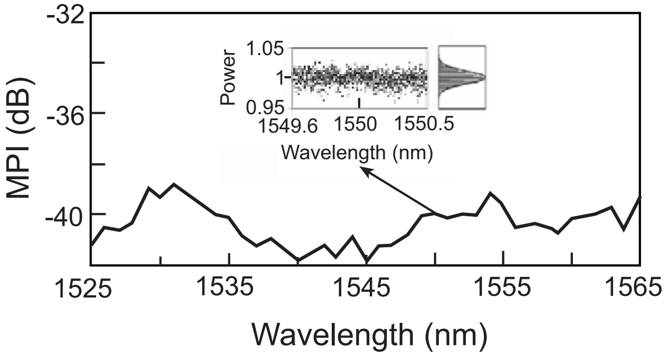

Fig. 32. MPI Measurement of a HOM-DCM for 100 km eLEAF compensation. Inset: 1300-point sample (and probability distribution) used for MPI measurement at 1550 nm.

the C-band into 1 nm windows, and calculating the MPI for each window, one can obtain the spectral dependence of the MPI with a 1-nm resolution. When using a swept wavelength system, care should be taken that the sweep rate is low enough so that the wavelength does not change significantly during the integration time of the detector. This can lead to an artificial reduction of the measured MPI, as discussed in [32].

Figure 32 shows results for a wavelength scanning MPI measurement of a HOM-DCM designed to compensate for 100 km of eLEAF transmission fiber. The inset of the figure shows the raw data (power as a function of wavelength, with four polarization states for each wavelength) used to calculate the MPI at 1550 nm. Also shown is the probability distribution function of the power fluctuations, which is well approximated by a Gaussian distribution, as noted above.

For a more detailed review of different aspects of MPI measurement in HOMF, see the work of Ramachandran and co-workers [32].

4.4. Sources of MPI in HOM-DCMs

In this section we discuss in more detail the various sources of MPI, and their relative contribution to the total MPI

4.4.1. Discrete Satellites

A discrete satellite is created when part of the signal energy is coupled to a HOMF mode other than the LP_{02} mode at the input MOX, propagates along the HOMF, and then is coupled back to the signal at the output MOX. By definition, only a single discrete satellite can exist for each guided mode within the HOMF (assuming all polarization states of the same mode are degenerate). As discussed in section 3.4.2.2, there are typically six guided modes within the HOMF: $LP_{01}, LP_{11}, LP_{21}, LP_{02}, LP_{12}$ and LP_{03}. The latter two modes are less guided than the LP_{02} mode, which means

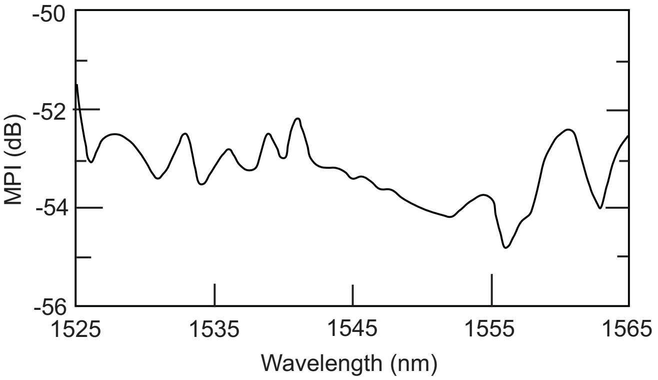

Fig. 33. MPI measurement of a "short" HOM-DCM, containing only 100 m of HOMF.

the HOMF can be designed to maximize the attenuation of these modes (if necessary with the aid of special attenuation loops, section 3.4.2.2) Therefore, in the context of discrete satellites we need only consider the three modes LP_{01}, LP_{11} and LP_{21},

If we designate the MOX extinction ratio with respect to mode i as η_i, then the power of the discrete satellite associated with this mode, relative to the power of the LP_{02} mode, is just η_i^2, where we have assumed that the input and output MOXes have the same extinction ratios (on average, this is a reasonable assumption). In Table 1 of section 2 we summarized results for the extinction ratios of the above three mode. This table shows that for a typical MOX the highest satellite power (usually that of LP_{01}) is about –45 dB, however, in the best case it can be as low as –52 dB.

The combined MPI from all three discrete satellites is then given by

$$\mathrm{MPI}_{\mathrm{discrete}} = \eta_{01}^2 + \eta_{11}^2 + \eta_{21}^2. \tag{34}$$

This value can be measured by constructing a HOM-DCM with a short ($\sim$100 m) length of HOM fiber. The short length of fiber means that mode coupling in the fiber is negligible, so the entire MPI of the HOM–DCM comes from discrete satellites. Fig. 33 shows an example of such a measurement over the C-Band, where it can be seen that the total MPI is below –51 dB over the entire band. This result is consistent with the best case values of the extinction ratios given in Table 1.

4.4.2. Continuous Satellites

Continuous satellites are created when coupling of the signal to an additional mode, and/or coupling back to the signal occurs due to mode coupling along the HOMF (See section 3.4.2.3 for a detailed discussion of mode coupling). Therefore, for each guided mode i(excluding the LP_{02} mode) in the HOMF, we identify three alternative processes for the creation of continuous satellites:

1. At the input MOX, power is coupled to the *i*th mode, and then part of this power is coupled back to the LP_{02} mode due to mode coupling along the HOMF.

2. As the signal propagates along the LP_{02} mode, power is coupled to the *i*th mode due to mode coupling, and then part of this is coupled back to the signal at the output MOX.
3. As the signal propagates along the LP_{02} mode, power is coupled to the *i*th mode due to mode coupling, and then is coupled back to the LP_{02} mode also due to mode coupling.

We refer to the first two processes as first order mode coupling, since each satellite created involves only a single mode-coupling event. Practically, these two processes are identical, and it is simple to show that the total satellite energy created by each is given by

$$\eta_i \int_0^L \kappa_i dx = \eta_i \kappa_i L, \tag{35}$$

where η_i is the MOX extinction ratio defined above, κ_i is the mode coupling coefficient between the LP_{02} mode and mode i as defined in section 3.4.2.3, and L is the HOMF length. We see that first order mode coupling can be reduced by improving the MOX extinction ratio η_i, and in theory can be eliminated entirely using ideal MOXes.

This is not the case for the third process, which we refer to as second order mode coupling. This process does not involve the MOXes at all, and occurs solely due to mode coupling. The total satellite power due to this process is given by

$$\int_0^L \kappa_i dx \int_x^L \kappa_i dy = \frac{1}{2} \left(\kappa_i L\right)^2, \tag{36}$$

i.e., it is quadratic in both the coupling coefficient and the fiber length. Since the process does not involve the MOXes, it cannot be reduced by improving MOX quality, and will exist even for ideal MOXes. Clearly one can consider higher order processes that involve more than two mode-coupling events. However, as long as $\kappa_i L \ll 1$, their contributions will be negligible compared to second order mode coupling.

As in section 4.4.1, we assume that the $\mathrm{LP}_{03}$and LP_{12} modes have high attenuation coefficients, so that we need only consider the LP_{01}, LP_{11}, and LP_{21} modes. From Table 4 in section 3.4.2.3 we see that the mode-coupling coefficient between LP_{02} and LP_{01} is typically much lower than the other two mode coupling coefficients, which leaves only 1st and 2nd order mode coupling involving LP_{11} and LP_{21}. Fig. 34 shows the (calculated) MPI due to 1st and 2nd order mode coupling involving these two modes, as a function of HOMF length. As can be seen from the figure, LP_{21} 2nd order coupling dominates for most relevant fiber lengths, although for lengths below 1.5 km the combined effect of LP_{11} and LP_{21} 1st order coupling can be greater.

4.4.3. Combined Contribution

Combining the various contributions discussed in sections 4.4.1 and 4.4.2, the total MPI may be written as

$$\mathrm{MPI} = \sum_{i=01,11,21} \left(\eta_i^2 + 2\eta_i \kappa_i L + \frac{1}{2} \left(\kappa_i L\right)^2 \right), \tag{37}$$

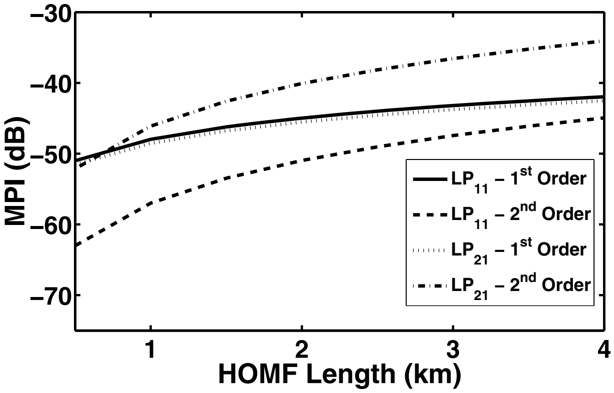

Fig. 34. MPI due to 1st and 2nd order mode coupling as a function of HOMF length. Typical MOX extinction ratios (Table 1) and mode coupling coefficients (Table 4) have been used in the calculation.

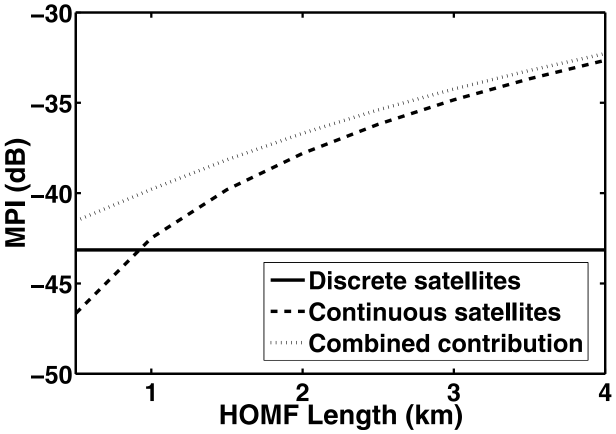

Fig. 35. MPI as a function of HOMF length from discrete and continuous satellites, and combined contribution.

where the η_i^2 terms represent discrete satellites, and all other terms represent continuous satellites. Figure 35 shows the relative contribution of discrete and continuous satellites to the total MPI for typical values of the various parameters. We see that for HOMF lengths of 1 km and above, the contribution from continuous satellites dominates the total MPI, while that of the discrete satellites becomes more and more negligible.

4.5. *Coherent and Incoherent MPI, and System Impact*

An important issue when considering the system impact of MPI is the time-scale of the power fluctuations. This is governed by the laser coherence time, τ_{coh}, which determines whether the MPI is coherent or incoherent [32–33]. If for a given satellite i, its relative delay with respect to that of the LP_{02} mode, $\Delta\tau_i$ (see Eq. (28) satisfies $\Delta\tau_i \ll \tau_{\mathrm{coh}}$, then the interference term due to that satellite is *coherent*, and will fluctuate with a time scale typical of the environmental changes in the system (usually a few seconds). On the other hand, if $\tau_{\mathrm{coh}} \ll \Delta\tau_i$, the interference term is *incoherent*, and will fluctuate with a timescale of the laser phase noise, i.e., τ_{coh}.

Since the laser sources used in long haul communication system typically have a linewidth, $\Delta\nu$, of a few MHz, τ_{coh} is usually in the range of 30–100 ns. Table 6 lists typical group delay values (per km HOMF) for the profile family discussed in section 3.4.1 (these values can be measured using a reflectometer setup as described in section 3.4.2.3). As the table shows us, $\Delta\tau_i <\sim \tau_{\mathrm{coh}}$, which means that MPI in HOM-DCMs can include both coherent and incoherent contributions, with the relative importance of each depending on the laser linewidth as well as the wavelength.

Table 6. Relative group delay per km between the LP_{02} mode and three other modes for the fiber profile family discussed in section 3.4.1. The range of group delay values corresponds to different wavelengths within the C-Band.

Mode	$\Delta\tau$ (ns/km)
LP_{01}	0–10
LP_{11}	5–20
LP_{21}	15–30

The system impact of coherent and incoherent MPI has been extensively studied both theoretically and experimentally [29–31,34–36]. In particular Ramachandran and co-workers [34], have studied the system impact of coherent distributed MPI, which is characteristic of HOM-DCMs.

When applying these results, the following should be remembered:

- The MPI as measured by the method described in section 4.3 is the total of coherent and incoherent MPI, and can thus be viewed as an upper limit for either contribution. For a discussion of separate measurement of coherent MPI in HOM-DCMs, see [32].
- The number of satellites contributing to MPI is large (see section 4.4), meaning that the distribution of power fluctuations due to MPI can be considered as Gaussian (see also Fig 32). This is particularly true when a number of HOM-DCMs are cascaded along a link. The Gaussian power distribution simplifies the theoretical analysis of MPI system impact, as well as the statistical treatment of coherent MPI power fluctuations [37].

4.6. *Summary*

MPI in HOM-DCMs is a relatively complex phenomenon, with multiple discrete and continuous sources and different timescales. In the preceding section we have discussed various aspects of the phenomenon, and characterized the nature of MPI in HOM-DCMs.

The MPI values of manufacturing grade HOM-DCMs are typically in the region of –36 to –40 dB. Various system tests to be described in section 5 have shown that these values are sufficiently low to allow virtually unimpaired ultra-long-haul transmission, in one case up to 6000k @ 10 Gb/s.

5. Applications of HOM-DCMs

In this section we consider the application of HOM-DCMs in modern optical networks. Specifically, we will show that despite the issue of MPI, HOM-DCMs can provide an excellent solution for dispersion management in many important cases.

5.1. Accurate Broadband Compensation

The widespread deployment in recent years of NZDSF has emphasized the need for a suitable broadband dispersion management solution that accounts for the large negative dispersion slope of these transmission fibers. In section 3.4 we showed how HOMF may be designed with the appropriate RDS for eLEAF® compensation, while maintaining a high effective area to minimize non-linear effects. Furthermore, in section 3.5, we discussed the option of adding a trim fiber to the HOM-DCM to fine-tune the dispersion and dispersion slope for accurate broadband compensation. While the discussion in section 3 focused on the design of HOMF for C-Band eLEAF® compensation, the same principles apply to the design of HOMF for other types of fiber and other transmission bands.

5.1.1. C-Band eLEAF® Compensation

Figure 36 shows the dispersion, MPI and insertion loss characteristics of a typical manufacturing grade HOM-DCM for compensation of 100 km eLEAF® transmission fiber. The maximum residual dispersion in the designed transmission band is 12 ps/nm, while the maximum MPI and insertion loss are –37.5 and 2.1 dB, respectively. Note that the insertion loss for this particular module is very low, due the fact that the insertion loss of the MOX'es is close to their ideal limit of about 0.8 dB/Mox (see section 2). Typically, the insertion loss for such a module would be in the range of 2.5–3.5 dB. Note also the very stable performance over a wide temperature range. The PMD of this particular module is 0.47 ps, which is more than sufficient for most applications.

The use of HOM-DCMs for C-Band eLEAF® compensation has been demonstrated in a number of 40G [38,39] and 10G [40] system experiments. In the latter, successful transmission was achieved over 2800 km, demonstrating that despite the issue of MPI, HOM-DCMs are an attractive solution even in ultra-long-haul (ULH) systems.

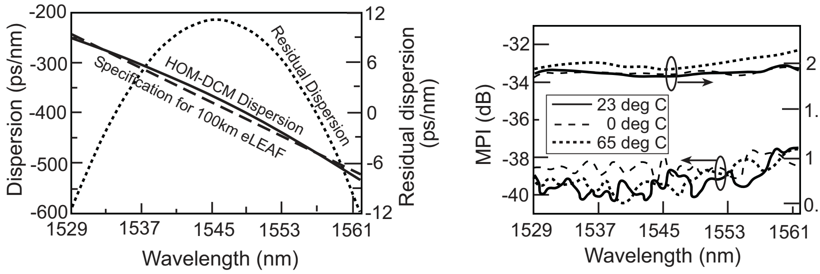

Fig. 36. Dispersion characteristics (left), and temperature dependent MPI and Insertion Loss (right) of a typical manufacturing grade HOM-DCM designed and built to compensate 100 km eLEAF® transmission fiber in the wavelength band 1529–1562 nm. The PMD of the HOM-DCM is 0.47 ps.

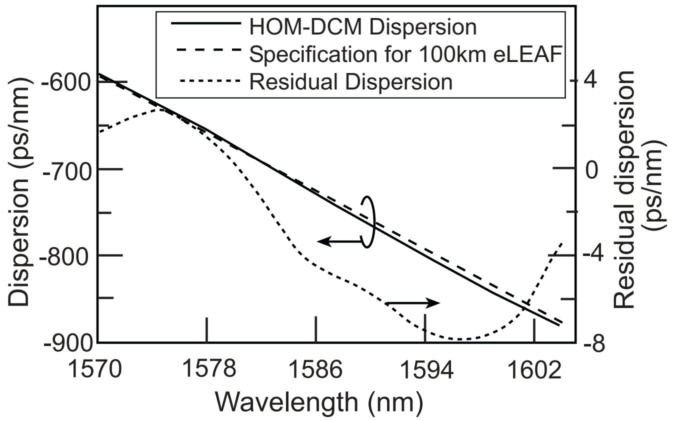

Fig. 37. Dispersion characteristics of a typical manufacturing grade HOM-DCM designed to compensate 100 km eLEAF® transmission fiber in the wavelength band 1570–1605 nm.

5.1.2. L-Band eLEAF® Compensation

The specified dispersion of eLEAF® transmission fiber at the center of the L-Band (1590 nm) is 7.6 ps/nm/km, while the dispersion slope is 0.085 ps/nm^2/km. On the one hand, this means that more HOMF is needed than in the C-Band in order to account for the larger dispersion. On the other hand, the RDS is lower than for the C-Band case, meaning that it's easier to achieve low TOD, and thus, low residual dispersion (see section 3.4.1.1).

This is illustrated in Fig. 37, which shows the dispersion curve of a manufacturing grade HOM-DCM designed to compensate for 100 km of eLEAF® transmission fiber in the wavelength band 1570–1605 nm. While the residual dispersion of the module is

8 ps/nm, it could easily be reduced to 5 ps/nm by fine-tuning the trim fiber within the module. Not only is the TOD much less than for a C-Band module ($\sim$1% compared to $\sim$3%), but the absolute residual dispersion is also less. The insertion loss of the module is 3.9 dB, which is more than a typical C-Band module due to the need for more HOMF. The maximum MPI of the module is –36 dB, which is about 2 dB worse than typically achieved values of more recent manufacturing series.

The above module together with others similar modules have been tested in a rigorous transmission test over 6000 km [41]. Despite the relatively high MPI of these modules, the results clearly show that MPI was not a limiting factor in the system. This illustrates once again that HOM-DCMs can be used in ultra-long-haul systems, and see also [42].

5.1.3. Other Transmission Fibers

In recent years, a new class of NZDSF fibers has been introduced, with the purpose to improve dispersion characteristics with respect to minimization of intra- and inter-channel non-linear effects, especially in high channel count WDM systems. The first such fiber to be introduced was Teralight® by Alcatel, and more recently True-wave reach® by OFS-Fitel [43], as well as others [44]. These fibers share common characteristics in that the dispersion at 1550 nm is typically 6–10 ps/nm/km, higher than previous generation NZDSF, but still significantly lower than SMF, while the RDS is typically in the range of 0.005-0.008 nm^{-1}, lower than previous generation NZDSF, but higher than SMF.

HOM-DCMs can also be manufactured to provide broadband compensation for these new NZDSFs, as well as for regular SMF fiber. A recent 2700-km, 40-Gb/s transmission test by Bissessur and co-workers [45] demonstrates the use of HOM-DCM for Teralight® compensation.

5.2. Reduced Nonlinear Penalty

As discussed previously, a key advantage of HOM-DCMs over conventional DCF is that the attractive dispersion properties of the HOMF can be achieved while maintaining a large modal effective area, typically above 50 μm^2 (compared to 20 μm^2 or less for DCF [46]). This, together with the small amount of HOMF in each device (below 3 km for most applications), significantly reduce the non-linear system penalty associated with HOM-DCMs.

A number of different tests [48–50] have directly demonstrated the increased power handling capabilities of HOM-DCMs over conventional DCF. With respect to cross phase modulation [47], it has been shown [48] that HOM-DCMs can tolerate almost 8 dB more power than commercially available DCF (with the same amount of dispersion). Furthermore, it was shown [49] that the HOM-DCM threshold to Brillouin scattering [47] is higher than 20 dBm, while that of commercially available DCF is as low 5 dBm. A system level test [50], also described in section 5.2.1 below, shows that HOM-DCMs can tolerate up to 13 dB more power for the same level of system penalty.

The increased power handling capability of HOM-DCMs is particularly important in high capacity systems, where non-linear effects tend to play a crucial role. This was first demonstrated for 40 Gb/s systems in a 1700-km transmission experiment using standard 100 km spans, and HOM-DCMs based on Bragg grating mode transformers [51]. Additionally, Killey and co-workers [39] have demonstrated how the improved power handling capabilities of HOM-DCMs can be utilized to minimize the overall non-linear penalty of 40 Gb/s systems. More recently, Bissessur and co-workers [45] have also utilized the power handling capability of HOM-DCMs in a novel 2700-km, 40-Gb/s test employing only single stage EDFA amplification. High density (25 and 50 GHz channel spacing) DWDM systems can also benefit from the reduced non-linear penalty of HOM-DCMs, as demonstrated by Meyer and co-workers [40] in a 2800-km, 25-GHz channel spacing, 10-Gb/s DWDM transmission experiment.

While the power handling capability of HOM-DCMs is most useful in next-generation high capacity systems, it can also be advantageous in current generation 10 Gb/s systems. Specifically, by optimizing the amplifier design to account for the properties of the HOM-DCMs placed at mid-stage, it is possible to improve the overall noise figure of the amplifier. This is briefly discussed in section 5.2.2 below.

5.2.1. System Level Comparison Between DCF and HOM-DCM

In this section we describe a system level test [50] designed to directly compare the power handling capabilities of HOM-DCMs and conventional DCF. Since the test involves only single channel transmission, inter-channel effects such as four-wave mixing and cross phase modulation [47] are not included. Furthermore Brillouin scattering is purposefully suppressed using phase dithering of the transmitter, leaving self-phase modulation as the main effect that is tested in the experiment.

The main components of the experimental setup are shown in Fig. 38. A 2^{23}–1 NRZ 10 Gb/s PRBS is transmitted through 80 km of SMF transmission fiber at a constant launch power of –4 dBm to minimize non-linear effects within the fiber. On the other hand, using Amp1 and Att1, the launch power into the DCM may be varied between –5 to +25 dBm. By varying the attenuation of Att2 and Att3, it is possible to change the OSNR (measured by the OSA) at the input to the receiver, while maintaining a constant receiver input power. The experimental procedure is as follows: For each value of launch power into the DCM, the OSNR at the receiver is changed until a specified BER is achieved. Since higher launch power means a larger non-linear penalty, it is necessary to increase the OSNR in order to maintain a fixed BER. The amount by which the OSNR must be increased quantifies the penalty.

Both the HOM-DCM and the commercially available DCF used in the experiment were designed to compensate the dispersion of 80 km SMF transmission fiber. Figure 39 shows the OSNR required to maintain a BER of 10^{-9} for different levels of DCM input power. The OSNR is given relative to the required OSNR at –5 dBm input power (i.e., negligible non-linear effects within the DCM). The results clearly illustrate that the HOM-DCM can tolerate up to 13 dB more input power for the same level of OSNR penalty, compared to the conventional DCF. This conclusion is further supported by the recorded eye diagrams, shown in the insets of Fig. 39. For the conventional DCF, the bit pattern exhibits clearly noticeable distortions for an input power of 13 dBm, whereas no such distortions can be seen for an input power of 21 dBm launched into the HOM-DCF.

It should be noted that the exact power tolerance advantage of HOM-DCMs over conventional DCF depends on the application. The more fiber (both HOMF and con-

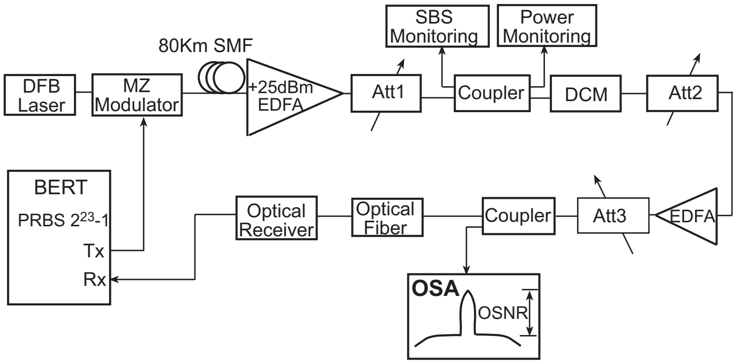

Fig. 38. Experimental setup used to compare the power handling capabilities of HOM-DCMs and conventional DCF.

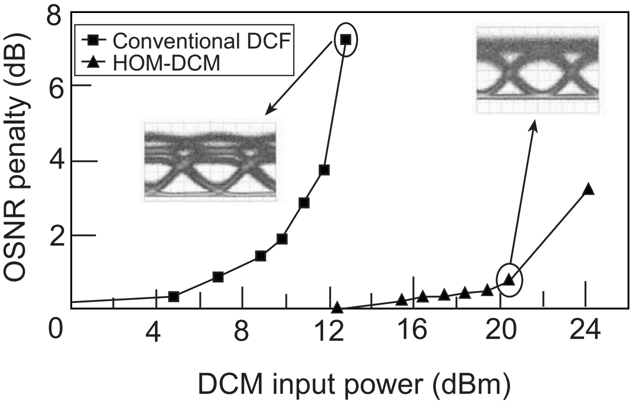

Fig. 39. The experimental results. Insets: transmitted eye diagrams corresponding to the marked input power.

ventional DCF) within the DCM, the larger the advantage of HOM-DCMs. Thus, systems using SMF transmission fiber will typically benefit more from HOM-DCMs (with respect to power tolerance) than systems employing NZDSF transmission fiber.

5.2.2. Using HOM-DCM to Optimize Amplifier Design

As illustrated in Fig. 40, in most conventional system designs DCMs are placed at the mid-stage of in-line amplifiers in each span. Current amplifier designs need to take into account the properties of conventional DCF, namely the low power tolerance and relatively high loss. The low power tolerance of the DCF means that the output power of the first amplification stage, the pre-amplifier, is restricted, which means that less of the total gain of the amplifier is assigned to the pre-amplifier, and more to the second amplification stage, the booster. The relatively high loss of the DCF also needs to be accounted for, since most amplifiers are optimized to work with a given *fixed* mid-stage loss. Thus, even if one uses a HOM-DCM with lower loss, it is often necessary to insert an attenuator to increase the total loss to that for which the amplifier is optimized.

The noise figure of a two-stage amplifier is given by (using linear quantities, not dB) [52]

$$\mathrm{NF} = \mathrm{NF}_{\mathrm{pre}} + \frac{\mathrm{NF}_{\mathrm{boost}}}{G_{\mathrm{pre}} T_{\mathrm{mid}}}, \tag{38}$$

where $\mathrm{NF}_{pre/boost}$ is the noise figure of the pre/booster amplification stage, G_{pre} is the gain of the pre-amplifier, and T_{mid} is the transmittance at the mid-stage. Assuming $\mathrm{NF}_{\mathrm{pre}}$ and $\mathrm{NF}_{\mathrm{boost}}$ remain constant, then one immediately sees that by increasing G_{pre} and T_{mid} (i.e., decreasing the mid-stage loss), it is possible to achieve an improvement in the noise figure of the amplifier as a whole.

By using a HOM-DCM for dispersion compensation, one may achieve both these goals, as illustrated in Fig. 40. Since the HOM-DCM can tolerate significantly more input power, G_{pre} may be increased, and in practice ceases to be limited by the HOM-DCM (it may be limited by available pump power and other factors). Furthermore, the reduced loss of the HOM-DCM allows the amplifier to be optimized for a much lower mid-stage loss, resulting in an increase of T_{mid} and a consequential decrease in the amplifier noise figure.

Clearly, the above arguments present a highly simplified picture, while amplifier design is a complex issue, far beyond the scope of this section. However, a detailed analysis supports the basic picture, and it can be shown that a 0.5–1 dB improvement in noise figure is obtainable using designs optimized for HOM-DCMs. This was demonstrated by the 40 Gb/s transmission test performed by Ramachandran and co-workers [51], where the improved amplifier noise figure was key to the ability to transmit over 1700 km using 100 km spans.

5.3. Additional Applications

In this section we describe additional applications of HOM-DCMs, which serve as examples as to how the advantages of the technology can open up new and advanced possibilities for system design. An example of this is a novel method for achieving tunable dispersion compensation using fiber based mode conversion and HOM fiber [53]. Other applications are described in more detail below.

5.3.1. HOM-DCMs for Multiple Span Compensation

One of the unique advantages of HOM-DCMs is the high figure of merit (FOM) of the HOMF, typically in the range of 800–1000 ps/nm/dB. However, this advantage is somewhat offset by the overhead loss of the MOXes, typically 0.7-1.3 dB/MOX. If for example we consider a HOM-DCM designed to compensate for 100 km eLEAF® transmission fiber, then the module loss will be 2.5–3.5 dB, with only ∼0.7 dB due to the HOMF, and the rest due to the MOXes. On the other hand, a HOM-DCM designed

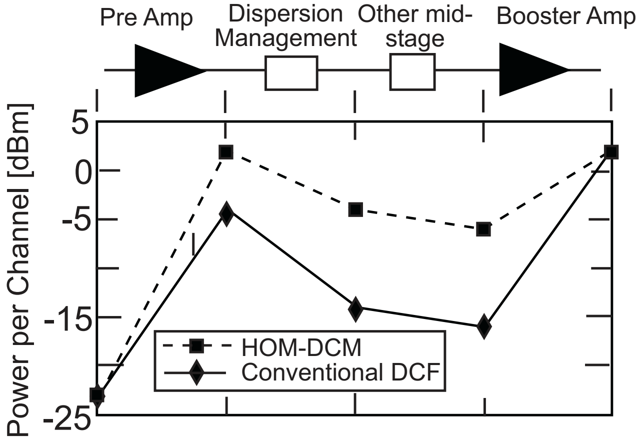

Fig. 40. Typical structure of a two-stage amplifier with mid-stage dispersion compensation. The solid line represents a typical EDFA design based on the relatively high loss and low power tolerance of conventional DCF, while the dashed line represent a possible improved design taking advantage of the HOM-DCM low loss and high power tolerance. The displayed power levels are for illustration purposes only.

to compensate for 200 km of eLEAF® will have 3.5–4.5 dB loss, since the MOX overhead remains changed. Thus, the longer the transmission span being compensated for, the more beneficial is the use of the high FOM HOMF, as illustrated in Fig. 41. This opens up an interesting possibility of using a single HOM-DCM to compensate for multiple spans [54], instead of using a single DCM in each span. This could potentially reduce system costs, since it would enable simpler, possibly single-stage amplifiers in the spans that do not include DCMs.

A potential limitation to this scheme is the MPI of the HOM-DCMs, as shown in Fig. 41. From this figure we see that a HOM-DCM for 400 km spans is expected to have 8 dB worse MPI than a corresponding HOM-DCM designed for 100 km spans. If on the other hand we were to concatenate four 100-km HOM-DCMs, then the MPI would be 6 dB worse than for a single 100-km HOM-DCM (see section 4.6.1). The extra 2 dB for the 400-km HOM-DCM results from the quadratic dependence of mode coupling on HOMF length, as discussed in section 4.4.2. For a 200-km HOM-DCM this is not an issue, since the MPI is expected to be similar to that of two 100-km HOM-DCMs (i.e., 3 dB worse).

Figure 42 shows insertion loss and MPI of a manufacturing grade HOM-DCM for compensation of 200 km eLEAF® spans. The maximum MPI of this module is –37.5 dB within the designed transmission band, which is better than the nominal –35 dB predicted in Fig. 41.

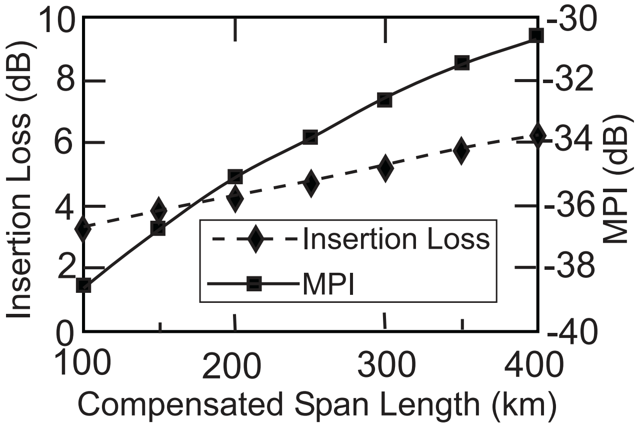

Fig. 41. Simulated MPI and Insertion loss of a HOM-DCM for compensation of eLEAF® fiber, as a function of compensated span length.

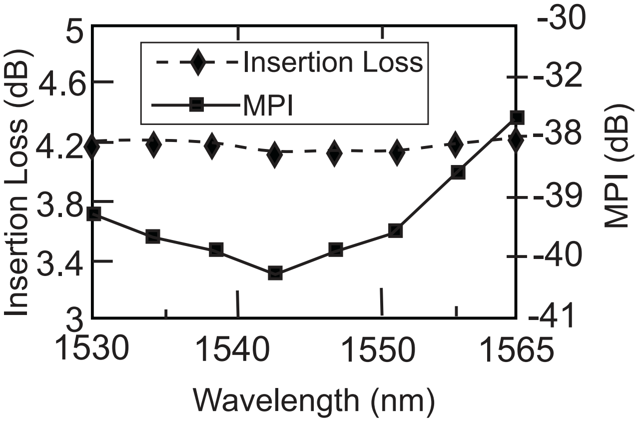

Fig. 42. Insertion loss and MPI of a manufacturing grade HOM-DCM for 200 km span eLEAF® compensation.

5.3.2. 160 GHz In-Channel Slope Compensation

Dispersion slope compensation is usually considered in the context of broadband WDM dispersion compensation. By achieving dispersion slope matching, one guarantees that if a single WDM channel is compensated for, the all other channels in the transmission band will also be compensated for. However, as bit rates grow, dispersion slope compensation also becomes important in the context of a *single* channel. If one has a residual uncompensated slope of δS at the receiver, then a non-negligible system penalty will be encountered if

$$\delta S \varDelta\lambda^2 \sim \tau_{\mathrm{bit}}, \tag{39}$$

where $\varDelta\lambda$ is the modulation-dictated spectral width of the channel, and $\tau_{\mathrm{bit}} \sim \lambda^2/\left(c\varDelta\lambda\right)$ is the time-slot of a single bit. Thus, in order to avoid significant penalty, the residual slope should satisfy

$$\delta S < \frac{\lambda^2}{c\varDelta\lambda^3}. \tag{40}$$

The cubic dependence on $\varDelta\lambda$ means that a 160-Gb/s channel is $\sim$4000 times more sensitive to residual slope than a 10-Gb/s channel, and $\sim$60 times more sensitive than a 40-Gb/s channel. Specifically, a 160-Gb/s C-Band channel can tolerate up to $\sim$2 ps/nm^2 residual slope. If one considers a 1000-km SMF link with total slope of 57 ps/nm^2, then this means that the slope compensation must be accurate to within better than 4%.

The ability to design HOMF with high dispersion slope opens up the possibility of producing specialized HOM-DCMs dedicated to dispersion slope compensation. The dispersion curve of such a module is shown Fig. 43, which shows that the dispersion at 1550 nm is close to zero, while the dispersion slope is 1.33 ps/nm^2. The HOM-DCM was constructed using $\sim$150m of HOMF with $D = -470$ ps/nm/km and $S = -10.2$ ps/nm^2/km, and $\sim$4.3 km of SMF fiber.

Fatome and co-workers [55] have demonstrated the usefulness of such a module in a 160-Gb/s transmission experiment over 900 km. In the absence of the HOM-DCM Slope compensator, it is estimated that the transmission distance would be reduced to $\sim$100 km.

5.3.3. Microwave Photonics True Time Delay Using HOM-DCM

Modern RF imaging systems are required to exhibit improved resolution, wider angular scans and bandwidths exceeding 10% of the RF carrier frequency. These requirements have led to the development of photonic True Time Delay (TTD) technology for beam steering/forming in phased array radars, as well as in other applications [56]. Soref [57] has suggested the use of chromatic dispersion in optical fibers to produce wavelength-dependent delay through $\varDelta\tau = DL\varDelta\lambda$, where $\varDelta\tau$ is the relative delay between two wavelengths, separated by $\varDelta\lambda$, D is the fiber dispersion coefficient, and L is the fiber length. A major problem with this method is the temperature drift of the RF phase, which is a direct consequence of the temperature dependence of the *optical* length of the fiber $d(n_{\mathrm{eff}}L)/dT(n_{\mathrm{eff}}$ is the effective refractive index of the propagating mode). Since this thermal sensitivity is proportional to L, maximizing the fiber dispersion, D, will minimize the fiber length L and its associated $d(n_{\mathrm{eff}}L)/dT$

Having a much higher dispersion coefficient, HOM-DCM have indeed been proven [58] to successfully implement photonic true time delay using much shorter fiber than equivalent DCF implementations, resulting in a three fold lower temperature dependence of the total delay. A possible issue of concern with HOM-DCMs is the effect of MPI on the transmitted RF signal. However, since to prevent walk-off [59],

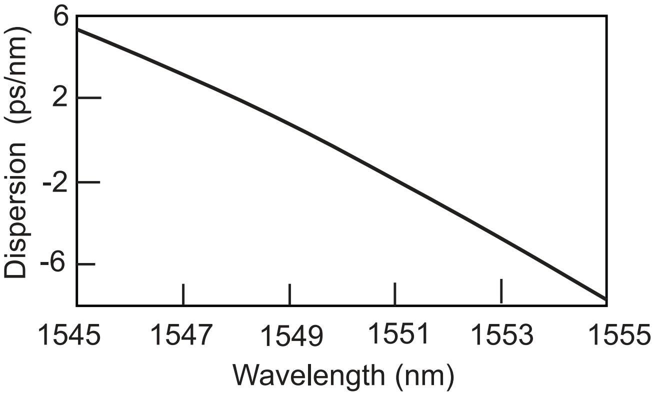

Fig. 43. Dispersion curve of a HOM-DCM dedicated to dispersion slope compensation. The module has close to zero dispersion @ 1550 nm, with a slope of 1.33 ps/nm^2.

the total dispersion in such applications is $\sim$100 ps/nm/km (for GHz applications), the length of HOMF is typically 200-300m, which means that mode coupling (see section 4. 4.2) is negligible. Thus, MPI values better than –40 dB can be achieved, resulting in negligible impact on the RF signal [58].

6. Summary

In this paper we have described in detail higher-order mode dispersion compensating modules (HOM-DCMs) based on spatial mode transformation technology. The combination of highly efficient spatial mode transformers (MOXes), together with carefully designed high-order mode fibers (HOMF), provides accurate broadband dispersion compensation, high power tolerance, and low insertion loss. While multi-path interference (MPI) remains a concern in HOM-DCMs, numerous system tests have demonstrated that currently achievable levels of MPI are sufficiently low to allow ultra-long-haul transmission.

The above properties make HOM-DCMs an attractive alternative in many applications in modern optical communications. Systems employing NZDSF transmission fiber especially benefit from HOM-DCMs, since it is relatively difficult to achieve broadband dispersion compensation using conventional DCF. The high power tolerance of HOM-DCMs provides important advantages in next generation high capacity systems, and can also be utilized in current generation systems to improve in-line amplifier performance. Other advanced applications, such as multi-span compensation, in-channel slope compensation for 160 Gb/s systems, and microwave Photonics, also benefit from the unique combination of HOM-DCM advantages.

Acknowledgement

The technological developments described in this paper, and their transformation into a manufacturable and field tested product, are the direct result of the dedication and talent of the entire LaserComm team.

References:

1. C.D. Poole, J.M. Wiesenfeld, A.R. McCormick, and K.T. Nelson, “Broadband dispersion compensation by using high-order spatial mode in a two-mode fiber”, Opt. Lett. **17**, 985–987 (1992).
2. C.D. Poole, J.M. Wiesenfeld, D.J. DiGiovanni, and A.M. Vengsarkar, “Optical fiber-based dispersion compensation using higher order modes near cutoff ”, J. Lightwave Technol. **12**, 1745–1758 (1994).
3. M. Eguchi, M. Koshiba, and Y. Tsuji, “Dispersion compensation based on dual-mode optical fiber with inhomogeneous profile core”, J. Lightwave Technol. **14**, 2387 (1996).
4. J.A. Buck, *Fundamentals of optical fibers* (John Wiley, 1995).
5. A.H. Gnauck and R.M. Jopson, “Dispersion compensation for optical fiber sytems”, in *Optical fiber Telelcommunications*, IIIA (Academic Press, 1997).
6. G.P. Agrawal, *Fiber-optic communication systems* (Wiley-Interscience, 1997).
7. H.G. Park and B.Y. Kim, “Intermodal coupler using permanently photoinduced grating in two-mode optical fibre”, Electron. Lett. **25**, 797–799 (1989).
8. S. Ramachandran, B. Mikkelsen, L.C. Cowsar, M.F. Yan, G. Raybon, L. Boivin, M. Fishteyn,W.A. Reed, P. Wisk, D. Brownlow, R.G. Huff, and L. Gruner-Nielsen, “All-fiber grating-based higher order mode dispersion compensator for broad-band compensation and 1000-km transmission at 40 Gb/s”, IEEE Photon. Technol. Lett. **13**, 632–634 (2001).
9. S. Ramachandran, Z. Wang, and M. Yan, “Bandwidth control of long-period grating-based mode converters in few-mode fibers”, Opt. Lett. **27**, 698 (2002).
10. S. Choi, W. Shin, and K. Oh, “Higher-order-mode dispersion compensation technique based on mode converter using hollow optical fiber”, in Proc. Optical Fiber Communication Conference 2002, pp. 177–178.
11. R. Oron, Y. Danziger, N. Davidson, A.A. Friesem, and E. Hasman, “Transverse Mode Selection with Phase Elements”, Conference on Lasers and Electro-Optics Europe (CLEO/Europe), p. 365, September 1998.
12. J.W. Goodman, *Introduction to Fourier Optics*, 2nd ed. (McGraw Hill, 1996).
13. M. Born and E. Wolf, *Principles of Optics*, 7th ed. (Cambridge University Press, 1999).
14. J. Bengtsson and M. Johansson, “Fan-out diffractive optical elements designed for increased fabrication tolerances to linear relief depth errors”, Appl. Opt. **41**, 281–289 (2002).
15. R.G. Dorsch, A.W. Lohmann, and S. Sinzinger, “Fresnel ping-pong algorithm for 2-plane computer-generated hologram display”, Appl. Opt. **33**, 869–875 (1994).
16. L. Gruner-Nielsen, S.N. Knudsen, B. Edvold, T. Veng, D. Magnussen, C.C Larsen, and H. Damsgaard, “Dispersion Compensating Fibers”, Opt. Fiber Technol. **6**, 164–180 (2000).
17. M.J. Li, “Recent progress in fiber dispersion compensators”, Paper Th.M.1.1., ECOC 2001, Amsterdam.

18. U. Levy and M. Tur, “Projected Zero Dispersion—A Concept for Link Design”, Tech. Digest of NFOEC 2002, p. 1527.
19. M. Wandel, T. Veng, Q. Le, and L. Grüner-Nielsen, “Dispersion compensating fibre with a high figure of merit”, Proceedings of 2001 European Conference on Optical Communications, Paper PD.A.1.4.
20. M. Wandel, P. Kristensen, T. Veng, Y. Qian, Q. Le, and L. Grüner-Nielsen, “Dispersion compensating fibers for non-zero dispersion fibers”, OFC 2002, Paper WU1.
21. Allan W. Snyder and John D. Love, *Optical Waveguide Theory* (Kluwer Academic, 1983).
22. D. Marcuse, “Bend loss of slab and fiber modes computed with diffraction theory”, IEEE J. Quantum Electron. **29**, 2957–2961 (1993).
23. D. Marcuse, “Microdeformation losses of single-mode fibers”, Appl. Opt. **23**, 1082 (1984).
24. A. Bjarklev, “Microdeformation losses of single-mode fibers with step-index profiles”, J. Lightwave Technol. **4**, 341 (1986).
25. C.B. Probst, A. Bjarklev, and S.B. Andreasen, “Experimental verification of microbending theory using mode coupling to discrete cladding modes”, J. Lightwave Technol. **7**, 55 (1989).
26. D Derickson, *Fiber Optic test and measurement* (Prentice-Hall, New Jersey, 1998).
27. J.A. Buck, *Fundamentals of optical fibers* (Wiley, New York, 1995).
28. L. Gruner-Nielsen, Yujun Qian, B. Palsdottir, P.B. Gaarde, S. Dyrbol, and T. Veng, “Module for simultaneous C+L-band dispersion compensation and Raman amplification”, Optical Fiber Communication Conference (OFC), TuJ6, Anaheim, California (2002)
29. J.L. Gimlet and N.K. Chaung, “Effects of phase to intensity noise generated by multiple reflection on Gigabit per second DFB laser transmission systems”, J. Lightwave Technol. **7**, 888 (1989).
30. S. Burtsev, W. Pelouch, and P. Gavrilovic, “Multi-path interference noise in multi-span transmission links using lumped Raman amplifiers”, Optical Fiber Communication Conference and Exhibit (OFC), TuR4, Anaheim, California (2002).
31. P.J. Legg, M. Tur, and I. Andonovic, “Solution paths to limit interferometric noise induced performance degredation in ASK/Direct detection lightwave networks”, J. Lightwave Technol. **14**, 1943 (1996).
32. S. Ramachandran, J.W. Nicholson, S. Ghalmi, and M. F. Yan, “Measurement of multipath interference in the coherent crosstalk regime”, IEEE Photon. Technol. Lett. **15**, 1171–1173 (August 2003).
33. Y. Shen, K. Lu, and W. Gu, “Coherent and incoherent crosstalk in WDM optical networks”, J. Lightwave Technol. **17**, 756 (1999).
34. S. Ramachandran, S. Ghalmi, J. Bromage, S. Chandrasekhar, and L.L. Buhl, “Evolution and Systems Impact of Coherent Distributed Multipath Interference”, IEEE Photon. Technol. Lett. **17**, 238 (2005).
35. H. Takahashi, O. Kazuhiro, and T. Hiromu, “Impact of crosstalk in an arrayed waveguide multiplexer on NxN Optical Interconnection”, J. Lightwave Technol. **14**, 1097 (1996).
36. C.X. Yu, W. Wang, and S.D.Brorson, “System degredation due to multipath coherent crosstalk in WDM network nodes”, J. Lightwave Technol. **16**, 1380 (1998).
37. S.D. Dods and A.J. Lowery, “Temporal Statistics of Crosstalk-Induced Errors in WDM Optical Networks”, NFOEC 2001, Session C5, pp. 876–879 (2001).
38. A.H. Gnauck, L.D. Garrett, Y. Danziger, U. Levy, and M. Tur, ‘Dispersion and dispersion-slope compensation of NZDSF over the entire C band using higher-order-mode fibre’, Electron. Lett. **35** (23), 1946–1947 (2000).

39. R.I. Killey, V. Mikhailov, S. Appathurai, and P. Bayvel, “Investigation of Nonlinear Distortion in 40-Gb/s Transmission With Higher Order Mode Fiber Dispersion Compensators”, J. Lightwave Technol. **20**, 2282 (2002).

40. C. Meyer, S. Lobo S, D. Le Guen, F. Merlaud, L. Billès, and T. Georges, “High spectral efficiency wideband terrestrial ULH RZ transmission over LEAF® with realistic industrial margins”, paper 1.1.2, ECOC 2002.

41. L.D. Garrett, M. Eiselt, J. Weisenfeld, R. Tkach, D. Menashe, U. Levy, Y. Danziger, and M. Tur, “ULH DWDM Transmission with HOM-Based Dispersion Compensation”, The 29th European Conference on Optical Communication (ECOC), Rimini, Italy, September 2003.

42. L.D. Garrett, M.H. Eiselt, J.M. Weisenfeld, M.R. Young, and R. Tkach, “Bidirectional ULH transmission of 160-gb/s full-duplex capacity over 5000 km in a fully bidirectional recirculating loop”, IEEE Photon. Technol. Lett. **16**, 1757–1759 (2004).

43. B. Zhu, L. Leng, L.E. Nelson, L. Gruner-Nielsen,Y. Qian, J. Bromage, S. Stulz, S. Kado, Y. Emori, S. Namiki, P. Gaarde, A. Judy, B. Palsdottir, and R.L. Lingle Jr., “3.2Tb/s (80 /spl times/ 42.7 Gb/s) transmission over 20 /spl times/ 100 km of non-zero dispersion fiber with simultaneous C + L-band dispersion compensation”, paper FC8, Optical Fiber Communication Conference and Exhibit, (OFC), 2002.

44. K. Mukasa, H. Moridaira, T. Yagi, and K. Kokura, “New type of dispersion management transmission line with MDF$^{\mathrm{SD}}$ for long-haul 40 GB/s transmission”, paper ThGG2, Optical Fiber Communication Conference (OFC), Anaheim, California, 2002.

45. H. Bissessur, A. Hugbart, C. Bastide, S. Gauchard, and S. Ruggeri, “Transmission of 32 × 43 Gb/s over 27 × 100 km of TeraLight fiber with low-cost EDFA amplification”, Paper ThE3, Optical Fiber Communication Conference (OFC), Los Angeles, California, 2004.

46. F. Forghieri, R.W. Tkach, and A.R. Chraplyvy, in "*Optical Fiber Telecommunications*, IIIA", edited by I.P. Kaminow and T.L. Koch, pp. 196–264 (Academic Press, 1997).

47. G.P. Agrawal, *Non-Linear Fiber Optics*, 2nd ed. (Academic Press, 1997).

48. M. Tur, E. Herman, and Y. Danziger, “Nonlinear properties of dispersion management modules employing high-order mode fibers”, Optical Fiber Communication Conference and Exhibit (OFC), TuS5-1-TuS5-3, (2001.

49. M. Tur, E. Herman, A. Kozhekin, and Y. Danziger, “Stimulated Brillouin Scattering in High-Order Mode Fibers Employed in Dispersion Management Modules”, IEEE Photon. Technol. Lett. **14**, 1282–1284 (2002).

50. O. Mor, B. Moav, A. Ben-Dor, M. Tur, S. Steinblatt, U. Levy, and D. Menashe, “Reduced nonlinearities in high order mode dispersion compensation modules”, The 7th European/French-Israeli Symposium on Nonlinear and Quantum Optics (EURISNO/FRISNO), Les Houches, France, February 2003.

51. S. Ramachandran, G. Raybon, B. Mikkelsen, A. Yan, L. Cowsar, and R.J. Essiambre, “1700 km transmission at 40 Gbit/s with 100 km amplifier spacing enabled by higher-order-mode dispersion compensation”, Electron. Lett. **37**, 1352–1354 (2001).

52. E. Desurvire, *Erbium-doped fiber amplifiers: principles and applications* (Wiley, 1994).

53. S. Ramachandran, S. Ghalmi, S. Chandrasekhar, I. Ryazansky, M. F. Yan, F. V. Dimarcello, W. A. Reed, and P. Wisk, “Tunable Dispersion Compensators Utilizing Higher Order Mode Fibers”, IEEE Photon. Technol. Lett. **15**, 727 (2003).

54. S. Ghalmi, S. Ramachandran, E. Monberg, Z. Wang, M. Yan, F. Dimarcello, W. Reed, P. Wisk, and J. Fleming, “Multiple Span Dispersion Compensation Using All-Fiber Higher Order Mode Dispersion Compensators”, The 28th European Conference on Optical Communication (ECOC), Paper P1.33, Copenhagen, Denmark, September, 2002.

55. J. Fatome, S. Pitois, P. Tchofo Dinda, and G. Millot, “Experimental demonstration of 160-GHz densely dispersion-managed soliton transmission in a single channel over 896 km of commercial fibers”, Opt. Express **11**, 1553–1558 (2003).
56. H. Zmuda and E.N. Toughlian, *Photonic Aspects of Modern RADAR* (Artech House, 1994).
57. R. Soref, “Optical dispersion technique for time-delay beam steering”, Appl. Opt. **31**, 7395–7397 (1992).
58. O. Raz, R. Rotman, Y. Danziger, and M. Tur, “Implementation of Photonic True Time Delay Using High-Order-Mode Dispersion Compensating Fibers”, IEEE Photon. Technol. Lett. **16**, 1367–1369 (May 2004).
59. J.L. Corral, J. Marti, and J.M. Fuster, “General Expressions for IM/DD Dispersive Analog Optical Links With External Modulation or Optical Up-Conversion in a Mach-Zehnder Electrooptical Modulator”, IEEE Trans. Microwave Theory Technol. **49**, 1958–1975 (2001).